INTERNATIONAL JOURNAL FOR NUMERICAL METHODS IN FLUIDS
Int. J. Numer. Meth. Fluids **30**: 357–405 (1999)

SENSITIVITY OF PLUME DYNAMICS TO THE PARAMETERIZATION OF VERTICAL MIXING

ALAN M. DAVIES* AND JIUXING XING

Proudman Oceanographic Laboratory, Bidston Observatory, Birkenhead, Merseyside, L43 7RA, UK

SUMMARY

A three-dimensional primitive equation, baroclinic numerical model incorporating a range of turbulence closure schemes is used to investigate the effects of vertical diffusion of momentum and density upon the spread of a freshwater plume, with particular reference to the Ebro plume. Initial calculations show that there are some differences in the horizontal spread and vertical mixing of the plume when diffusion coefficients are computed from a two-equation turbulence energy model compared with a one-equation model. To understand results from the turbulence energy models, the sensitivity of the plume dynamics to variations in the coefficient of vertical eddy viscosity and diffusivity is also considered, with increases in these parameters having a significant effect upon the cross-shore and along-shore spread of the plume. Also, increasing these parameters changes the plume characteristics from supercritical to subcritical and reduces the occurrence of meandering and baroclinic instability along the plume's off-shore edge. However, differences in the southerly spread (the direction of Kelvin wave propagation in the model) of the plume (although not its northerly spread) produced by changes in diffusion coefficients are small compared with the influence of changes in the bottom slope, upon the along-shore southerly spread of the plume, which moves in the direction of Kelvin wave propagation in the near coastal region. Results from the series of calculations are used as a guide in experimental design, with reference to a planned experiment in the Ebro region involving a coastal HF Radar deployment, as well as off-shore measurements. Calculations suggest that surface current measurements from a coastal HF Radar, together with a detailed survey of the density field associated with the plume, may be an appropriate, although indirect, means of determining suitable mixing coefficients to use in plume discharge problems. Detailed measurements of water depth variation will also be required. Copyright © 1999 John Wiley & Sons, Ltd.

KEY WORDS: plume; vertical mixing; Ebro River; topography; stratification

1. INTRODUCTION

In coastal regions, fresh water from river outflows is discharged into a region of more saline, and hence higher density, sea water. The fresh water spreads as a surface buoyant layer (a river plume) away from the discharge point, and forms an off-shore bulge and a coastal current with an associated plume front spreading along the coast in the direction of Kelvin wave propagation. The basic dynamics controlling the movement of river plumes, namely the role of

---

* Correspondence to: Proudman Oceanographic Laboratory, Bidston Observatory, Birkenhead, Merseyside, L43 7RA, UK.

Contract/grant sponsor: EC MAST Research Programme, Directorate General for Science, Research and Development; Contract/grant number: MAS3-CT95-0037, DG12-ESCY

CCC 0271–2091/99/120357–49$17.50

Received November 1997
Revised March 1998

the magnitude of the river discharge, rotational effects and the importance of the non-linear terms in determining the off-shore and along-shore spread of the plume and baroclinic instabilities along the plume front have been known for some time, e.g. [1–3].

Although a number of observational programmes have been undertaken to examine flows in near coastal regions, e.g. [4,5], which have confirmed the general features of the spreading of surface plumes, and a number of numerical modelling studies have been carried out, e.g. [6–9], the role and importance of vertical mixing of momentum and density upon the large scale plume dynamics has never been investigated in detail.

In this paper, as a precursor to a large modelling and observational programme in the region of the Ebro River outflow into the western Mediterranean (Figure 1), the authors perform such an investigation. In order to clearly identify the role of vertical mixing, the sea region (the Balearic Sea) adjacent to the Ebro discharge is represented by a rectangular domain open on all boundaries, except the land boundary, which is adjacent to the Spanish Coast (Figure 1), and the off-shore boundary, near the shelf edge. Since the off-shore spread of the plume is

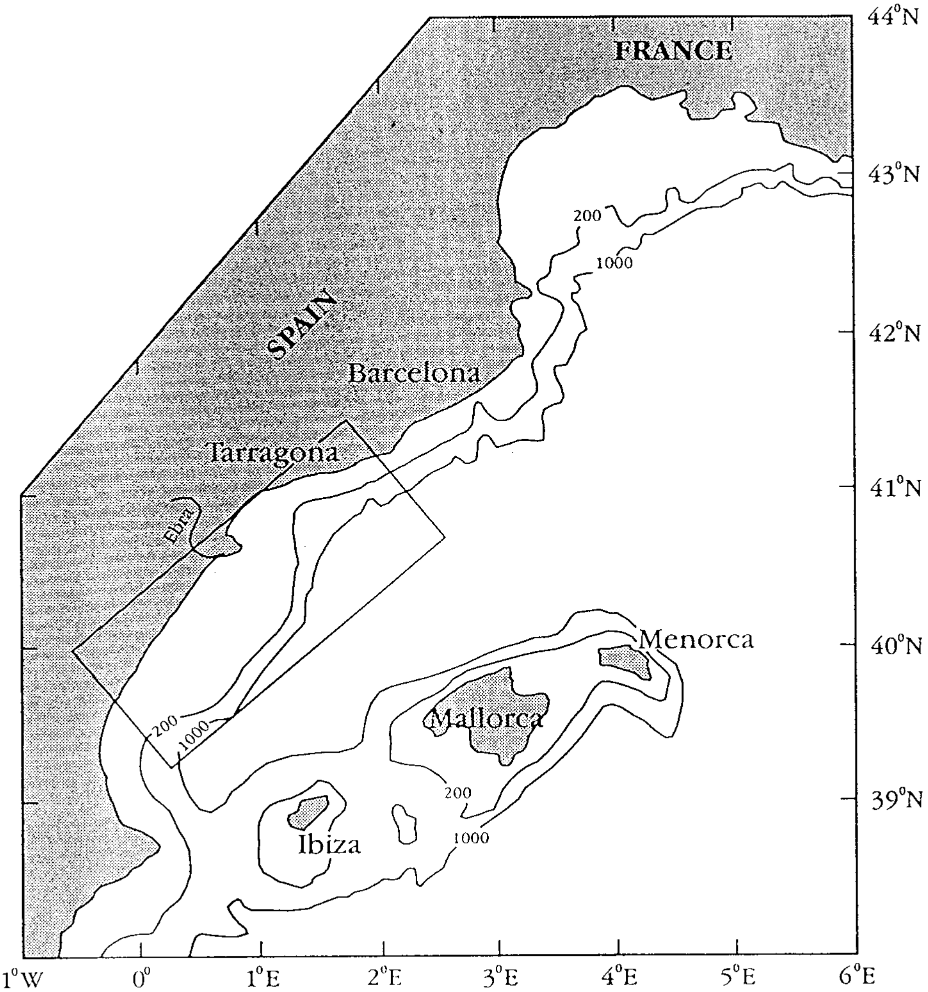

Figure 1. Schematic showing the location of the Balearic Sea and the idealized model used in the calculations.

confined to the near shore region, the form of the shelf edge boundary does not influence the solution. An idealized depth distribution is assumed in the region in order to examine the relative roles of diffusion and depth upon the spread of the plume. Although the Balearic Sea region has a large scale circulation controlled by thermo-haline and wind effects [10–14] in the coastal regions, it receives a major input of fresh water from the rivers, with a significant input from the Ebro [15]. This fresh water gives rise to a shelf break salinity front that separates the on shelf water from that in deeper water.

The primary aim in this paper is to examine the importance of vertical mixing in determining the off-shore and along-shore spread of the Ebro plume, and how this influences the surface flow fields associated with the plume. The relative importance of changes in the parameterization of vertical mixing compared with the effects of bottom topography upon the spread of the plume will also be considered. The emphasis here on surface flow fields is because this modelling work is designed to guide a field measurement programme, an important part of which will be the use of a shore based HF Radar system to measure surface currents in the region of the Ebro discharge. The HF Radar system is ideally suited to the measurements of surface currents, for which it can provide a detailed horizontal spatial distribution that cannot be achieved from conventional current meter deployments. The system has proved to be very valuable in measuring the small scale but intense jet-like currents associated with frontal dynamics [16].

The numerical calculations presented here, show that there is significant spatial variability in the surface currents associated with the spread of the Ebro plume. Consequently, measurements made with the HF Radar system are essential in studying the spatial variability of this spread. As will be shown, there are a number of factors influencing the fine scale features of the plume movement, and a combination of surface measurements and modelling will be required to determine the role of each. However, preliminary process-type modelling of the form presented here can be used to identify the critical measurements that need to be made. In this paper the authors concentrate on the role of vertical mixing of both momentum and density in determining the spread of the plume. They examine this by considering a number of parameterizations of vertical mixing of both momentum and density using both one-equation and two-equation turbulence energy models. To understand the relative importance of the parameterizations of vertical diffusion of momentum and density within these models, the authors will also consider a number of calculations using fixed eddy viscosity and diffusivity values. The discharge of the Ebro plume is ideally suited to such a sensitivity study in that unlike many other river discharges (e.g. the Rhine [9]), there are no strong tidal currents to advect the plume and enhance its vertical mixing.

To first order the discharge of a river plume typically consists of an off-shore bulge and a coastal current in the direction of Kelvin wave propagation. In the case in which the width of the bulge is greater than the width of the coastal current, the plume will be classified as being supercritical [7]. Such a plume often exhibits a meandering pattern along its frontal edge, caused by baroclinic instability as it propagates away from the discharge point. In the case in which the width of the coastal current, at its widest point, is greater than the width of the bulge, the plume is classed as subcritical, and the meandering pattern is absent. As will be shown here, for a given discharge rate and density difference between the fresh water discharge and the more saline sea water, the Ebro plume exhibits both supercritical and subcritical features depending upon the parameterization of vertical mixing of both density and momentum. Consequently, the surface discharge features of the plume, as measured by HF Radar, combined with field measurements of density, may prove to be an important test of the accuracy of various parameterizations of vertical mixing in three-dimensional models. The classification of plumes described above is very convenient in the series of calculations being considered here, in which the density difference between the plume discharge and the sea water is constant. Also, the plume discharge rate is fixed, and the sea water is at rest, and hence any differences in the spreading of the plume are related to the pararmeterization of vertical mixing. In the inviscid limit theories, e.g. [17], it is suggested that the internal Froude number (Fr), which may be defined as the ratio of the discharge velocity V_D at the estuary mouth, to the speed of internal gravity waves $C_I = \sqrt{g'h}$ [with $g' = (\Delta\rho/\rho_0)g$, with ρ_0 the mean density and $\Delta\rho$ the density difference between two layers (e.g. surface fresh water, and lower saline water)] may be the parameter controlling whether a plume is supercritical ($Fr > 1$) or subcritical ($Fr < 1$). However, since we are dealing here with vertical mixing of both density and momentum, and the density difference in the vertical varies significantly from point to point and through time, as does the velocity of the plume away from the discharge point, then the use of the Froude number classification is not particularly helpful.

The three-dimensional numerical model employed in the calculations and the numerical method used to solve the hydrodynamic equations are briefly presented in the next section. In subsequent sections of the paper, results from a series of calculations designed to determine the role of vertical mixing and bottom topography upon the spatial extent of the Ebro plume, are presented.

2. THREE-DIMENSIONAL NUMERICAL MODEL

Since the region under consideration is relatively small, namely a rectangular domain of 250 km north–south by 110 km west–east, the hydrodynamic equations are written in a Cartesian co-ordinate in the horizontal, with a sigma co-ordinate in the vertical, thus,

2.1. Hydrodynamic equations

$$\frac{\partial Hu}{\partial t} + \nabla\cdot(Hu\vec{V}) + \frac{\partial Hu\omega}{\partial\sigma} - fHv = -gH\frac{\partial\zeta}{\partial x} + \mathrm{BPF}_x + \frac{1}{H^2}\frac{\partial}{\partial\sigma}\left(A_v\frac{\partial Hu}{\partial\sigma}\right) + HF_u, \tag{1}$$

$$\frac{\partial Hv}{\partial t} + \nabla\cdot(Hv\vec{V}) + \frac{\partial Hv\omega}{\partial\sigma} + fHu = -gH\frac{\partial\zeta}{\partial y} + \mathrm{BPF}_y + \frac{1}{H^2}\frac{\partial}{\partial\sigma}\left(A_v\frac{\partial Hv}{\partial\sigma}\right) + HF_v, \tag{2}$$

$$\frac{\partial\zeta}{\partial t} + \nabla\cdot\left(\int_{-1}^{0}(H\vec{V})\,\mathrm{d}\sigma\right) = 0, \tag{3}$$

$$\frac{\partial HS}{\partial t} + \nabla\cdot(HS\vec{V}) + \frac{\partial HS\omega}{\partial\sigma} = \frac{1}{H^2}\frac{\partial}{\partial\sigma}\left(K_v\frac{\partial HS}{\partial\sigma}\right) + HF_S, \tag{4}$$

$$\frac{\partial P}{\partial\sigma} = -\rho gH, \tag{5a}$$

with density ρ related to the salinity using [18]

$$\rho = 1000.0 + \sigma_t, \tag{5b}$$

where $\sigma_t = 28.152 - 0.0735T - 0.00469T^2 + (0.802 - 0.002T)(S - 35)$ with temperature T assumed to be 10°C.

In the hydrodynamic equations, the sigma co-ordinate is defined by

$$\sigma = (z - \zeta)/H, \tag{6}$$

with, $\vec{V}=(u, v)$ and (u, v, ω) are the velocity components corresponding to the (x, y, σ) co-ordinates; ρ is density; S is the salinity; H is the total water depth; ζ is the elevation of the sea surface above the undisturbed level; z is the water depth increasing vertically upwards with $z=h$, the free-surface and $z=-h$, the sea bed; f is the Coriolis parameter, g is the gravitational acceleration; t is time; A_v and K_v are vertical eddy viscosity and diffusivity coefficients; F_u, F_v and F_S are horizontal diffusions for the momentum and salinity; P is the pressure field. In these equations, the baroclinic pressure force terms (BPF_x, BPF_y) are given by

$$\mathrm{BPF}_x=-\frac{H}{\rho_0}\frac{\partial P_{\mathrm{b}_0}}{\partial x}\bigg|_z-\frac{H}{\rho_0}\left(\frac{\partial(P_{\mathrm{b}}-P_{\mathrm{b}_0})}{\partial x}+\frac{\sigma}{H}\frac{\partial(P_{\mathrm{b}}-P_{\mathrm{b}_0})}{\partial\sigma}\frac{\partial H}{\partial x}+\frac{1}{H}\frac{\partial(P_{\mathrm{b}}-P_{\mathrm{b}_0})}{\partial\sigma}\frac{\partial\zeta}{\partial x}\right), \tag{7}$$

$$\mathrm{BPF}_y=-\frac{H}{\rho_0}\frac{\partial P_{\mathrm{b}_0}}{\partial y}\bigg|_z-\frac{H}{\rho_0}\left(\frac{\partial(P_{\mathrm{b}}-P_{\mathrm{b}_0})}{\partial y}+\frac{\sigma}{H}\frac{\partial(P_{\mathrm{b}}-P_{\mathrm{b}_0})}{\partial\sigma}\frac{\partial H}{\partial y}+\frac{1}{H}\frac{\partial(P_{\mathrm{b}}-P_{\mathrm{b}_0})}{\partial\sigma}\frac{\partial\zeta}{\partial y}\right), \tag{8}$$

where P_{b_0} is a reference baroclinic pressure or the initial baroclinic pressure field. The first terms on the right-hand-side of Equations (7) and (8) are the pressure forces calculated using the z co-ordinate. In this way errors due to the co-ordinate transformation [19,20] can be reduced. The horizontal diffusion terms F_u, F_v and F_S in Equations (1), (2) and (4) are parameterized with a biharmonic horizontal term. Considering the term F_u for illustrative purposes, the biharmonic form is given by

$$F_u=-B_m\nabla^4 u=-B_m\left(\frac{\partial^4 u}{\partial x^4}+2\frac{\partial^4 u}{\partial x^2\,\partial y^2}+\frac{\partial^4 u}{\partial y^4}\right), \tag{9}$$

with B_m the constant horizontal diffusion coefficient having a value of 1.0×10^8 ($\mathrm{m}^4\,\mathrm{s}^{-1}$). For salinity and turbulent energy (see later) the diffusion coefficients are denoted B_h. In the calculations considered later, identical horizontal diffusion coefficients for salinity, turbulence and momentum were used. The more scale selective filtering properties of the biharmonic form of the horizontal diffusion operator are considered in Heathershaw *et al.* [21].

A time splitting method is used to integrate the hydrodynamic equations in order to reduce the computational time, in which the depth mean currents (external mode) are separated from the depth-dependent velocity (internal mode). The vertical velocity ω can be computed diagnostically using the continuity equation [22].

A staggered Arakawa C uniform finite difference grid is used in the horizontal with a variable grid in σ co-ordinates in the vertical. The vertical diffusion terms that are computed using turbulence energy models, (see later) are computed by a semi-implicit time integration method in order to avoid the use of a short time step when a fine grid is used in the vertical. Details of the method can be found in [23–26].

2.2. The two-equation turbulence energy model (2-eqn tke model)

The determination of the vertical eddy viscosity and diffusivity is accomplished using the well-established approach given by Blumberg and Mellor [27] and Oey and Chen [28,29], which involves prognostic equations for the turbulence energy and mixing length, which can then be used in the computation of viscosity and diffusivity. (The model is commonly referred to as a q^2-q^2l model). A similar approach has been used by Baumert and Radach [30], although they use prognostic equations for turbulence energy and dissipation rate.

The equations for this turbulence energy model in sigma co-ordinates are given by

$$\frac{\partial q^2 H}{\partial t} + \nabla\cdot(Hq^2\vec{V}) + \frac{\partial Hq^2\omega}{\partial\sigma}$$
$$= 2\frac{A_v}{H}\left[\left(\frac{\partial u}{\partial\sigma}\right)^2 + \left(\frac{\partial v}{\partial\sigma}\right)^2\right] + \frac{2gK_v}{\rho_0}\frac{\partial\rho}{\partial\sigma} - \frac{2q^3H}{B_1 l} + \frac{1}{H^2}\frac{\partial}{\partial\sigma}\left(S_q q l\frac{\partial q^2 H}{\partial\sigma}\right) + HF_q \tag{10}$$

and

$$\frac{\partial q^2 l H}{\partial t} + \nabla\cdot(Hq^2 l\vec{V}) + \frac{\partial Hq^2 l\omega}{\partial\sigma}$$
$$= \frac{lE_1A_v}{H}\left[\left(\frac{\partial u}{\partial\sigma}\right)^2 + \left(\frac{\partial v}{\partial\sigma}\right)^2\right] + \frac{lE_1gK_v}{\rho_0}\frac{\partial\rho}{\partial\sigma} - \frac{q^3}{B_1}WH + \frac{1}{H^2}\frac{\partial}{\partial\sigma}\left(S_q q l\frac{\partial q^2 l}{\partial\sigma}\right) + HF_l. \tag{11}$$

In these equations $q^2 = 2E$ with E the turbulence kinetic energy and l the mixing length. The wall proximity function W and the various coefficients S_q, B_1, E_1, are as defined in [27].

The diffusion coefficients for momentum A_v (namely eddy viscosity) and density K_v (namely eddy diffusivity) are computed from

$$A_v = lqS_M, \qquad K_v = lqS_H, \tag{12}$$

with the algebraic form of the stability functions S_M and S_H identical to those used by Galperin *et al.* [31,32], and will not be presented here. A limiting condition [32] is applied to l, of the form

$$l \le \frac{k_1 q}{N}, \tag{13}$$

with k_1 a specified constant [9,33] and N the Buoyancy frequency.

2.3. A one-equation turbulence energy model (1-eqn tke model)

In this model, the eddy viscosity A_v and eddy diffusivity K_v are computed from the turbulence energy E, derived from a single prognostic equation, and the mixing length l is given algebraically.

The turbulence energy E is computed from

$$\frac{\partial E}{\partial t} = A_v\left\{\left(\frac{\partial u}{\partial z}\right)^2 + \left(\frac{\partial v}{\partial z}\right)^2\right\} + \beta_0\frac{\partial}{\partial z}\left(A_v\frac{\partial E}{\partial z}\right) + \frac{gK_v}{\rho_0}\frac{\partial\rho}{\partial\sigma} - \varepsilon, \tag{14}$$

where ε is the turbulence dissipation is given by

$$\varepsilon = C_0C_1E^2/A_v, \tag{15}$$

with

$$K_v = A_v = C_0 l E^{1/2}, \tag{16}$$

where $\beta_0 = 0.73$, $C_0 = C^{1/4}$, $C_1 = C_0^3$, where $C = 0.046$ [34].

The mixing length l can be determined either in terms of an integral of the turbulence energy [35–38] or using an algebraic expression. A simple algebraic form of the mixing length that has been used in a number of calculations [25,26,39,40] is given by

$$l = 1/\left(\frac{1}{l_1} + \frac{1}{l_2}\right), \tag{17}$$

with

$$l_1 = K(\sigma H + H + z_0)\exp(\beta_1 \sigma) \tag{18}$$

and

$$l_2 = K(z_s - \sigma H), \tag{19}$$

with $K = 0.4$ the Von Karman constant, β_1 an empirical coefficient, $H = h + \zeta$ the total depth of water, and σ normalized vertical co-ordinate, with z_0 the bed roughness length, and z_s a surface roughness length, which controls the value of l at the sea surface.

2.4. Boundary conditions

At sea surface and sea bed there is no salinity flux, thus

$$\left.\frac{\partial S}{\partial \sigma}\right|_0 = 0, \qquad \left.\frac{\partial S}{\partial \sigma}\right|_{-1} = 0. \tag{20}$$

At the sea surface, the internal stress is set equal to the externally applied wind stress components τ_x and τ_y. In the case of buoyancy forcing only (the problem considered here), the surface stress is zero.

$$\rho \left.\frac{A_v}{H}\frac{\partial u}{\partial \sigma}\right|_0 = \tau_x, \qquad \rho \left.\frac{A_v}{H}\frac{\partial v}{\partial \sigma}\right|_0 = \tau_y. \tag{21}$$

Although here we are only concerned with the influence of mixing and water depth variations upon the spread of the plume, the wind influence is ignored. At the sea bed, a quadratic bottom friction condition is applied of the form,

$$\left.\frac{A_v}{H}\frac{\partial u}{\partial \sigma}\right|_{-1} = C_d u_h (u_h^2 + v_h^2)^{1/2}, \qquad \left.\frac{A_v}{H}\frac{\partial v}{\partial \sigma}\right|_{-1} = C_d v_h (u_h^2 + v_h^2)^{1/2}, \tag{22}$$

with u_h and v_h components of bed current, and C_d a coefficient of bottom friction determined from

$$C_d = \left[\frac{K}{\ln(z_r/z_0)}\right]^2, \tag{23}$$

with $K = 0.4$ the Von Karman constant, z_0 the bed roughness, and z_r the reference height above the bed at which C_d and the currents u_h and v_h are computed.

In a turbulence energy submodel for plume flows, the vertical flux of turbulence energy or $q^2 l$ is zero at the sea surface. With a slip condition at the bed, the sea bed turbulence energy boundary condition includes the balance of turbulence production, dissipation and diffusion. Since details are given in the literature [26] they will not be repeated.

At land boundaries, a no-flow condition normal to the land was assumed, except at the location of the Ebro discharge (see later) and along open boundaries a radiation condition for the flow fields with a flow relaxation zone [41] for the other variables was applied.

3. CALCULATIONS WITH A CONSTANT WATER DEPTH

3.1. Model domain

In this series of calculations, the region near the Ebro outflow is represented by a rectangular domain (Figure 1) with the western side aligned with the coast. The rectangle has dimensions of 250 km north–south and 110 km west–east and is closed along its western side to represent the coast of Spain. The eastern off-shore boundary is also closed although within the integration period considered here (of order 20 days) and the area of interest (the Ebro Delta), this boundary does not influence the solution. All other boundaries are open. A uniform finite difference grid with a 2 km spacing west–east and 3 km north–south is used in the horizontal, with 25 sigma levels in the vertical. A finer spacing is employed in the near surface layer in order to resolve the vertical density gradients associated with the buoyant plume. An internal mode time step of 600 s was used, with an external mode time step a factor of 40 smaller. The Coriolis parameter was set at 10^{-4} s^{-1}. The horizontal grid spacing is sufficiently fine to resolve the internal Rossby radius of deformation, and accurately represent the small scale features of the plume dynamics in the region downstream from the discharge point. The discharge of the Ebro water is represented as a point source of fresh water [salinity 5 ppt (parts per thousand)], located 180 km north of the southern end of the basin. Since idealized topography is used in the calculation, the location of the Ebro outflow is arbitrary. A position 180 km north of the southern boundary was chosen so that within the initial integration period, during which the plume was evolving and spreading, it would be contained within the region (see later discussion). Similarly, by choosing the eastern boundary sufficiently far from the source, the plume was not affected by this boundary. In all calculations considered here, the salinity of the oceanic water into which the fresh Ebro plume discharged was set at 35 ppt (parts per thousand), with the discharge rate fixed at 2000 m^3 s^{-1}. These are typical values for the area with the discharge rate close to its maximum value.

In the series of calculations presented in this paper, this discharge rate and density difference are fixed, and the sensitivity of the Ebro plume to the parameterization of vertical mixing is examined, initially in a region of constant water depth and subsequently with a sloping sea bed.

3.2. Flat bottom $h = 20$ m, A_v and K_v computed with the 1-eqn tke model (calculation 1)

In an initial calculation (calculation 1, Table I), water depths were constant everywhere at 20 m, and the vertical mixing of density and momentum was computed using the 1-eqn tke model.

Contours of surface salinity after 15 days following the discharge (Figure 2(a)i) show a characteristic bulge in the region of the outflow. In the case of a constant velocity, taken as the discharge velocity V_D, ignoring non-linear terms and frictional effects, the extent of this bulge is given by the inertial radius of deformation, namely $|V_D|/f$ [3]. Surface currents show a near surface gyre in the vicinity of the discharge, with an along-coast flow producing a southerly spreading of the plume, the geographical extent of which will be denoted by the 34 ppt contour. Of particular interest is the wave-like meandering of the outer edge of the plume, primarily due to baroclinic instability. Since the horizontal shear is large at the frontal edge of the plume, barotropic instability could also play a role in producing this wave-like meandering. Associated with these meanders there is significant spatial variability in the currents, with regions of strong surface current occurring in areas of maximum salinity gradient, suggesting first-order to a local geostrophic balance. The large bulge at the discharge point and the southward extent of the plume are characteristic of a supercritical plume. Surface elevation contours (Figure 2(a)ii) show a small increase in surface elevation in the region of the plume, which shows a similar spatial variability to that found in the surface salinity distribution and flow field. The surface elevation distribution is in near geostrophic balance with the depth mean current that exhibits a clockwise eddy in the vicinity of the discharge point with a series

Table I. Summary of parameters used in the calculations and relevant sections and figures

Calculation	Section in text	Relevant figures	Water depth	Mixing
Calculations with a constant depth				
1	3.2	2(a)–(c)	20 m (constant)	1-eqn tke
2	3.3	3(a)–(c)	20 m (constant)	2-eqn tke
3	3.4	4(a)–(b)	20 m (constant)	$A_v = 0.001$ m^2 s^{-1} $K_v = 0.0001$ m^2 s^{-1}
4	3.5	5(a)–(b)	20 m (constant)	$A_v = 0.001$ m^2 s^{-1} $K_v = 0.0005$ m^2 s^{-1}
5	3.6.1	6(a)–(b)	20 m(constant)	$A_v = 0.005$ m^2 s^{-1} $K_v = 0.0001$ m^2 s^{-1}
5R	3.6.2	6(c)–(d)	20 m (constant)	$A_v = 0.005$ m^2 s^{-1} $K_v = 0.0005$ m^2 s^{-1}
Calculations with depth increasing with distance from shore				
6	4.1	7(a)–(c)	Varying (20 m coast)	1-eqn tke
7	4.2	8(a)–(b)	Varying (20 m coast)	$A_v = 0.001$ m^2 s^{-1} $K_v = 0.0001$ m^2 s^{-1}
8	4.3	9(a)–(b)	Varying (20 m coast)	$A_v = 0.001$ m^2 s^{-1} $K_v = 0.001$ m^2 s^{-1}
9	4.4	10(a)–(b)	Varying (20 m coast)	$A_v = 0.001$ m^2 s^{-1} $K_v = 0.00001$ m^2 s^{-1}
10	4.5	11(a)–(b)	Varying (20 m coast)	$A_v = 0.0001$ m^2 s^{-1} $K_v = 0.0001$ m^2 s^{-1}
11	4.6	12(a)–(b)	Varying (20 m coast)	$A_v = 0.0001$ m^2 s^{-1} $K_v = 0.001$ m^2 s^{-1}
12	4.7	13(a)–(b)	Varying (10 m coast)	$A_v = 0.001$ m^2 s^{-1} $K_v = 0.0001$ m^2 s^{-1}
13	4.8	14(a)–(b)	Varying (10 m coast)	$A_v = 0.001$ m^2 s^{-1} $K_v = 0.001$ m^2 s^{-1}

of meanders and eddies to the south of this. It is evident from Figure 2(a)i and (a)ii that the depth mean current is a factor of three or four times smaller than the surface flow.

Salinity contours along a cross-section (C_1) just south of the discharge point extending to 50 km perpendicular to the coast show low salinity surface water close to the coast, with salinity increasing with depth in the near coastal region (Figure 2(b)). The low salinity water spreads off shore as a buoyant surface plume with the front of this plume (denoted by the 34 ppt contour), having extended approximately 30 km off shore at the surface and 25 km at the sea bed within the first 15 days. The off-shore spreading of salinity is not uniform, due to the near surface circulation produced by rotational and buoyancy effects, with a small core of salinity at 6 ppt trapped by the surface eddy shown in Figure 2(a)i.

Contours of the u component of the current (Figure 2(b)) show that there is an on-shore movement of water mainly confined to a surface layer of about 10 m thickness with the maximum shoreward velocity occurring at about 5 km from the coast. This corresponds to the on shore flow that can be seen in Figure 2(a)i at the southern edge of the eddy located at 175 km. However, as can be clearly seen from Figure 2(a)i, the position of this maximum is very sensitive to the exact north–south location of the cross-section compared with the discharge point. Below mid-depth, the direction of the u current reverses, reaching a maximum off-shore flow of 5 cm s^{-1} at 15 m below the surface, with current magnitudes decreasing in the near bed layer due to frictional effects.

Contours of the v component of the velocity (Figure 2(b)) show the maximum southerly flow occurring at the surface at approximately 25 km from the coast with the current reducing to zero below this surface layer. Close to the coast, beneath the surface layer there is a northerly near shore return flow of comparable magnitude with the surface flow, corresponding to an undercurrent that moves more dense water northward to compensate for the southward propagation of the surface plume. At approximately 8 km there is a northerly flow throughout the water column, with a southerly surface flow between this point and the coast. From Figure 2(a)i, it is apparent that the magnitude and horizontal distribution of the v velocity is influenced by small changes in the position of the cross-section relative to the discharge point.

Contours of the vertical component of velocity (Figure 2(b)), show a down welling region within 10 km of the coastline. This is responsible for the vertical advection of the fresh water in the region of the discharge point, which produces the sharp vertical salinity gradient found in the near shore region and the more uniform distribution extending out to 15 km from the coast, where the vertical velocity is near zero and horizontal advection dominates. Contours of turbulence energy (Figure 2(b)) show a maximum in the surface layer close to the coast where the vertical variation of the current and hence the shear production term is large, and the vertical density gradient, namely the buoyancy term that suppresses turbulence, is small. Although there is significant vertical shear in the v component of the velocity at 25 km off shore there is no surface turbulence energy maximum at this location. This is probably because the u component of the velocity is much less, and the vertical density gradient that suppresses turbulence is much stronger here than in the near shore region. Turbulence energy increases rapidly close to the bed, within 20 km of the coastline, where the flow in the bottom boundary layer is significant and hence the shear production term is strong. The enhanced vertical mixing that this produces in the bottom boundary layer, within 20 km of the coastline, explains the presence of the well-mixed near bed layer in this region.

The spatial distribution of the turbulence energy is reflected in the distribution of eddy viscosity, with eddy diffusivity showing an identical variation. The magnitude of the eddy viscosity is on average small, although in regions of significant turbulence it exceeds 0.001 $m^2 s^{-1}$.

Salinity and velocity contours at cross-section C_2 (Figure 2(c)), located to the south of the discharge point (at a position 145 km from the southern end of the region), show a surface fresh water wedge with the plume front (taken as the 34 ppt contour) only extending approximately 10 km off shore. The u velocity contours show an on-shore advection at all depths, corresponding at the surface to the on-shore flow shown in Figure 2(a)i and there is no evidence of the off-shore flow at depth found at cross-section C_1. Contours of the v velocity show a southerly flow in the upper part of the water column, which moves the plume down the coast, with a northerly flow of water in the bottom boundary layer. A similar distribution of the vertical velocity contours to that found at cross-section C_1 is evident, although the magnitude of the velocity is reduced. Turbulence energy values and eddy viscosity values (not shown) are comparable with those along cross-section C_1.

Figure 2. (a) Horizontal spatial distribution of (i) salinity contours (ppt) and surface currents (ii) surface elevation and depth mean currents in a subdomain of the model, 15 days after the discharge of the fresh water plume, computed with the one-equation model (calculation 1). (b) Contours after 15 days of salinity (ppt), u, v and w ($\times 10^{-3}$) components of velocity (cm s^{-1}), turbulent kinetic energy ($\log_{10}$, $m^2 s^{-2}$) and viscosity ($\log_{10}$, $m^2 s^{-1}$) at cross-section C_1 just south of the discharge point. (Note a dashed line represents a negative value with the zero line denoted by a dashed and dotted curve.) (c) As (b) (but without turbulent kinetic energy or viscosity contours) but at cross-section C_2 located at 150 km from the southern boundary of the model.

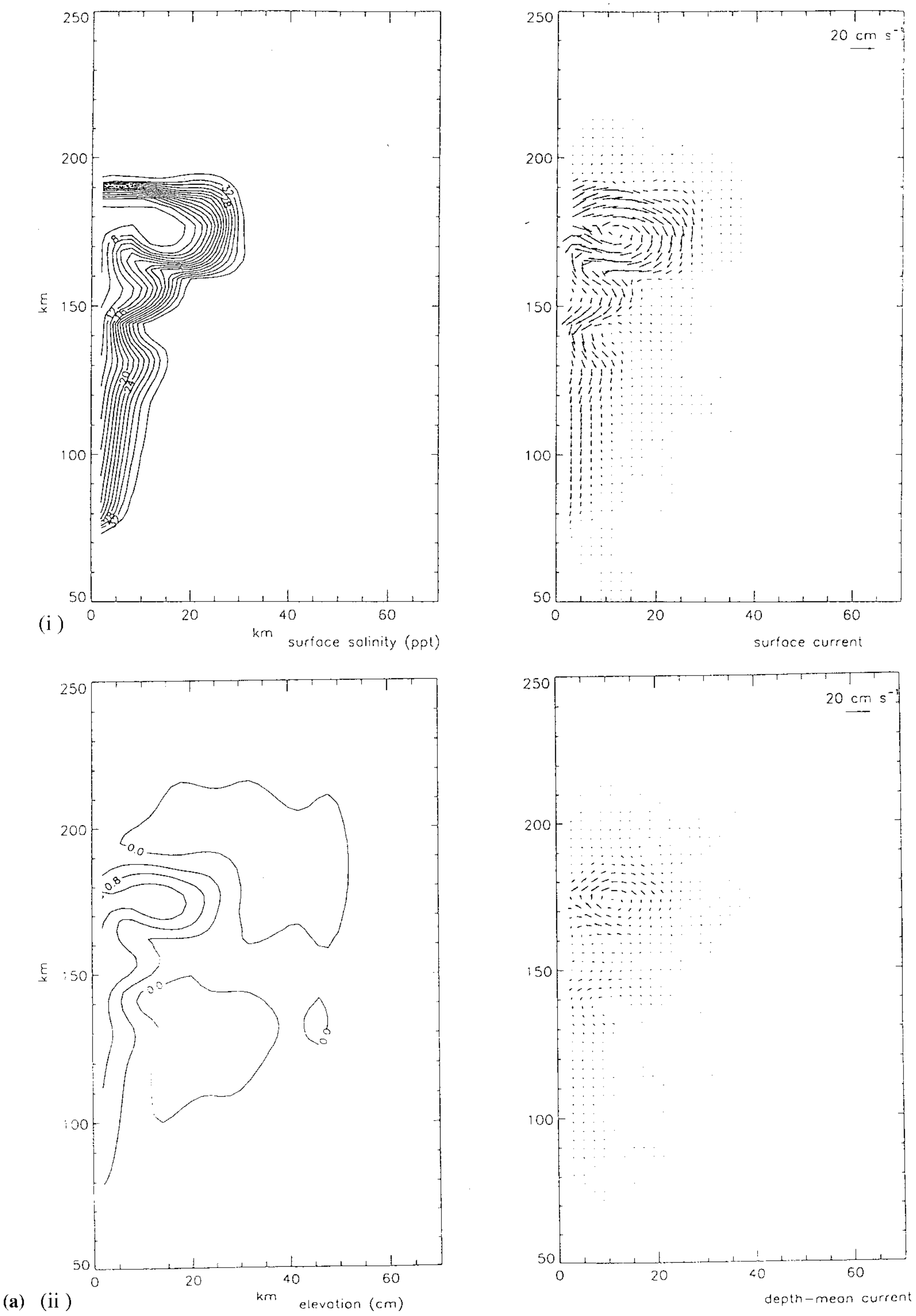
(i)
(a) (ii)
km
surface salinity (ppt)
surface current
elevation (cm)
depth−mean current
20 cm s⁻¹
250
200
150
100
50
0
20
40
60
0.0
0.8

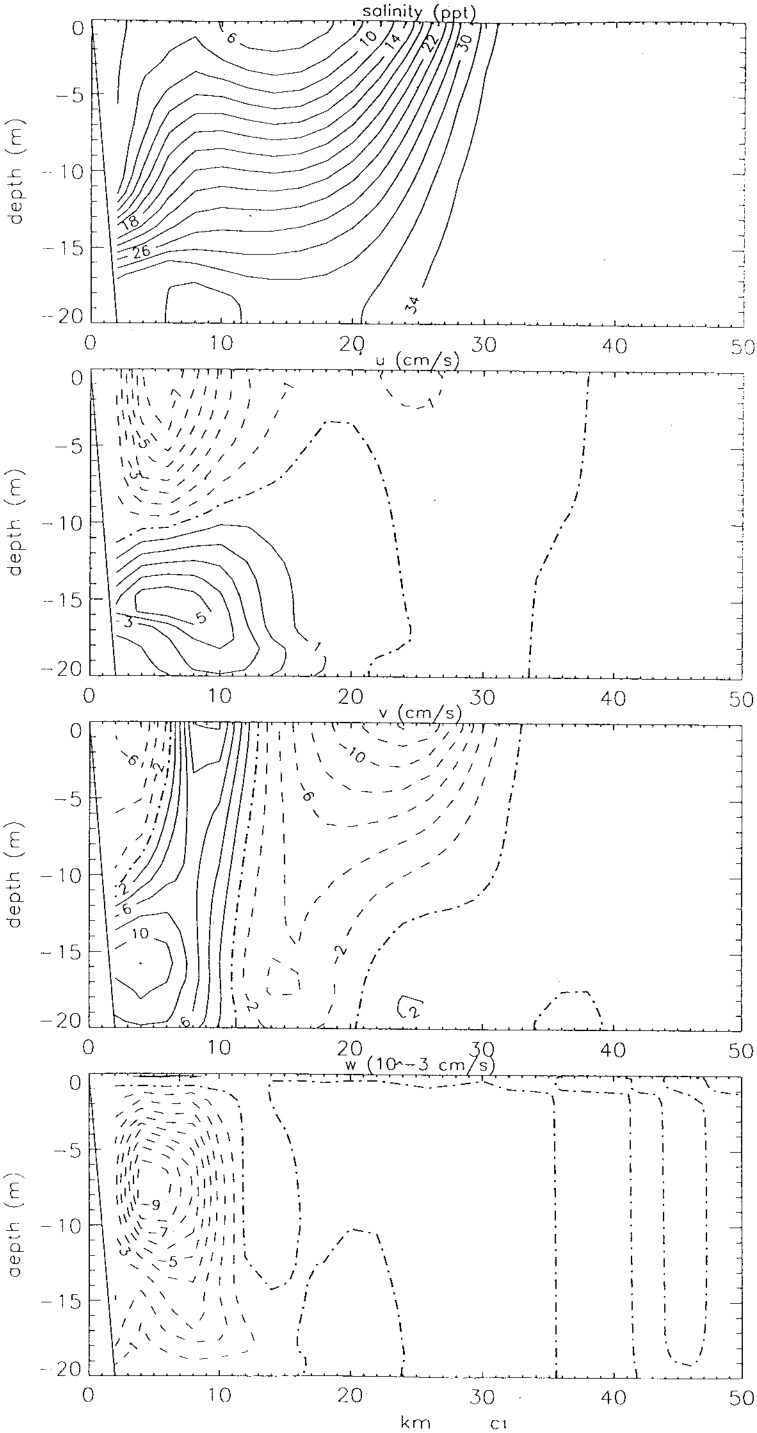

Figure 2 (*Continued*)

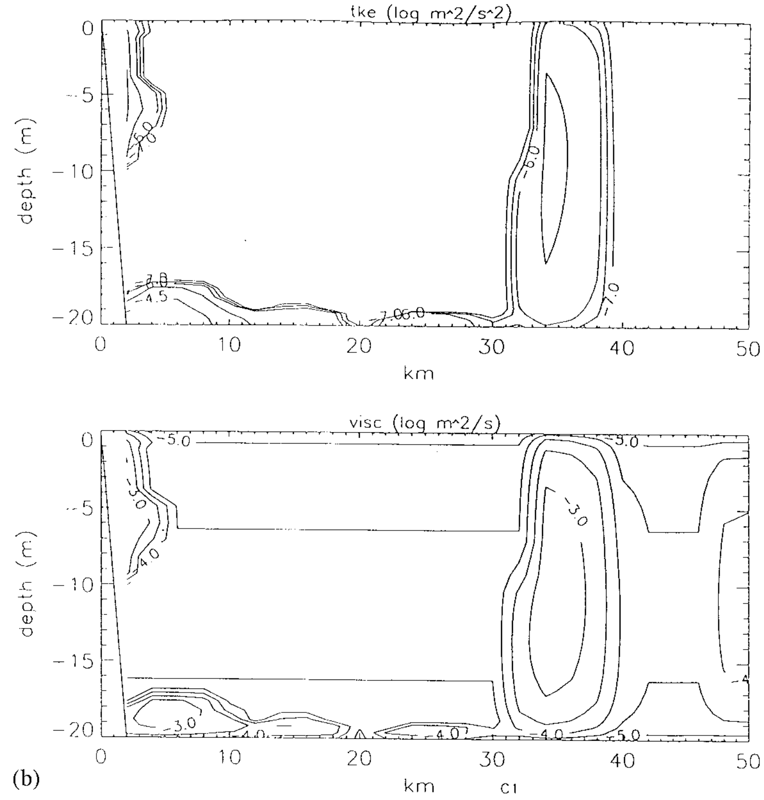

Figure 2. (*Continued*)

3.3. Flat bottom $h = 20$ m, A_v and K_v computed with the 2-eqn tke model (calculation 2)

In a subsequent calculation (calculation 2, Table I), the 2-eqn tke model was used to parameterize the vertical mixing. From a comparison of salinity distributions and surface currents computed with the two-equation (Figure 3(a)) and one-equation (Figure 2(a)) turbulence models, it is clear that the southerly extent of the plume is slightly larger using the two-equation model with the off-shore extent near the discharge point having a more circular front than before. As previously, the plume is supercritical. Although the spatial distribution of surface currents is similar in both cases, the off-shore extent is slightly reduced in calculation 2, with current magnitudes slightly larger than found previously. Similar small differences are evident in the spatial distributions (not shown) of surface elevations and depth mean currents. The fact that the plume has spread further south, with a comparable off-shore spread, suggests that it is more of a surface plume than that found in calculation 1. The surface nature of the plume is clearly evident from the salinity profiles given in Figures 3(b) and (c).

From a comparison of salinity contours along cross-section C_1, it is evident that although the off shore position of the 34 ppt contour is comparable in both cases, in calculation 2 this contour has not reached the sea bed, and the plume is confined to the near surface layer. Although the major features of the spatial distributions of the u and v components of current are comparable in both calculations (cf. Figure 2(b) and Figure 3(b)), there are some differences, particularly in the near shore region, which lead to a reduction in the vertical component of velocity.

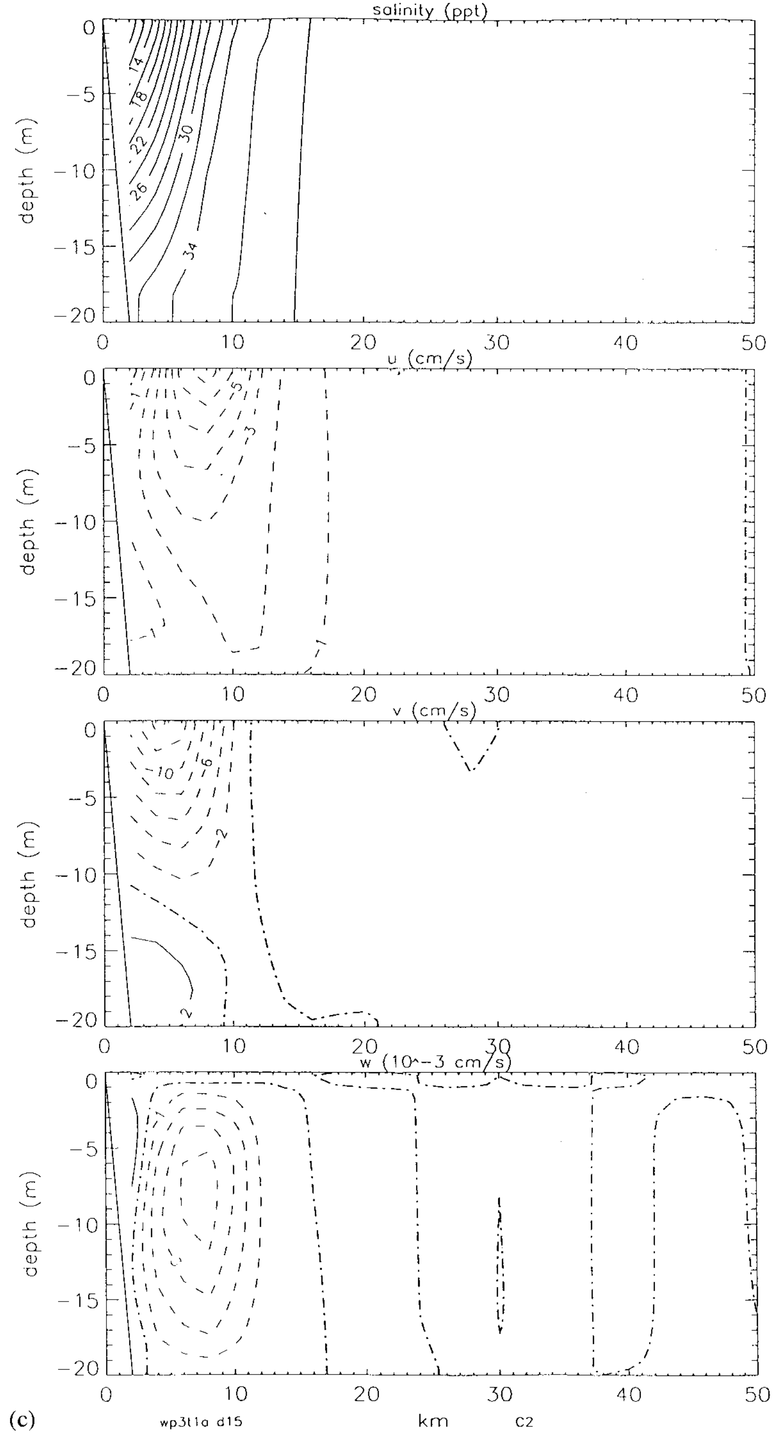

Figure 2 (*Continued*)

Contours of turbulence energy and viscosity (not shown) exhibit similar spatial features to those found previously, although on average, the two-equation turbulence model leads to slightly lower viscosity and diffusion values to those found with the one-equation model. The main reason for the reduced diffusion coefficients in the two-equation model, is that the buoyancy term in Equation (11) reduces the magnitude of the mixing length in regions of strong vertical density gradient (this is clearly illustrated in [26]). Since A_v and K_v in the two-equation model are related to the magnitude of the mixing length (Equation (12)), they are significantly reduced in the region of strong vertical gradients. However, in the one-equation model, the mixing length is specified algebraically (Equation (17)) and is not reduced by stratification effects and hence A_v and K_v tend to be larger than in the two-equation model. An alternative form of the mixing length in the one-equation model is to use Equation (17) to determine an initial mixing length, which is then modified by a weighting function depending upon the local Richardson number. Such an approach produces a reduction in the mixing length comparable with that found in the two-equation model [42]. This method and other forms of turbulence closure approach are discussed briefly in the conclusions section.

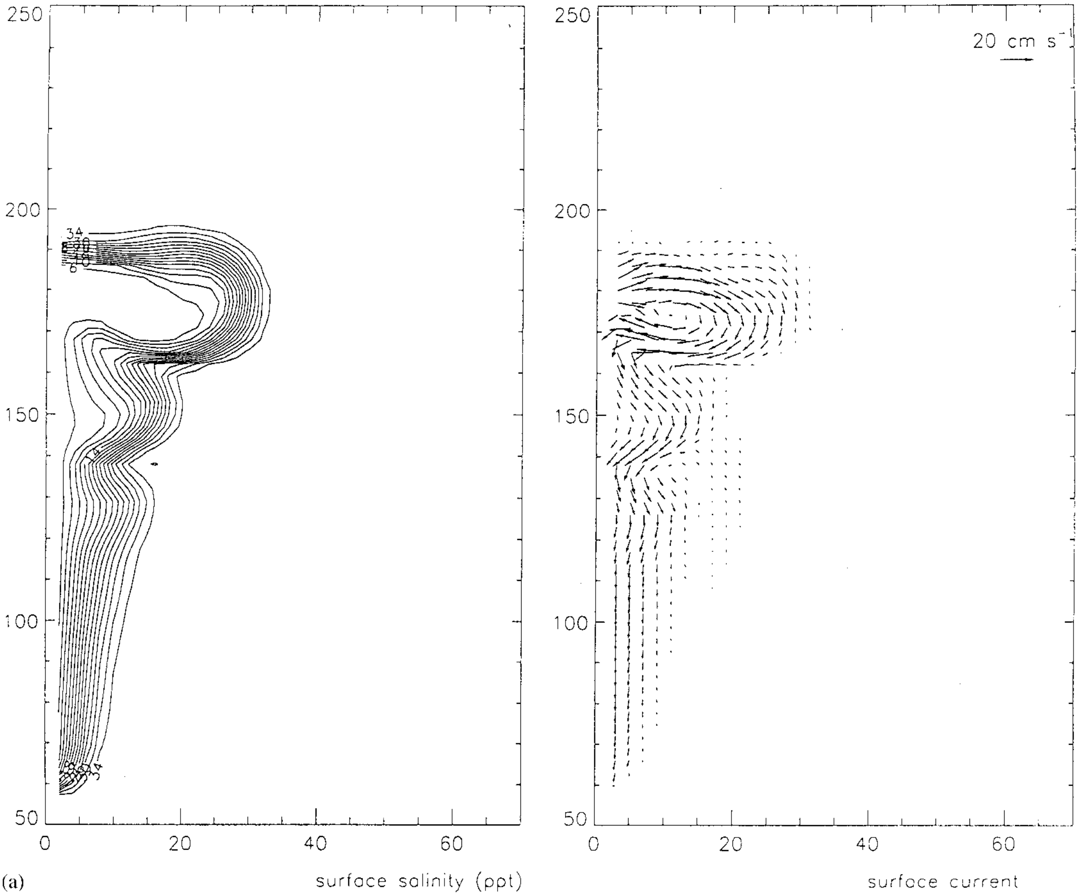

Figure 3. (a) Horizontal spatial distribution of (i) salinity contours (ppt) and surface currents in a subdomain of the model, 15 days after the discharge of the fresh water plume computed with the two-equation model (calculation 2, Table I). (b) Contours after 15 days of salinity (ppt), u, v and w ($\times 10^{-3}$) components of velocity (cm s^{-1}), at cross-section C_1 from calculation 2, Table I. (c) As (b) but at cross-section C_2.

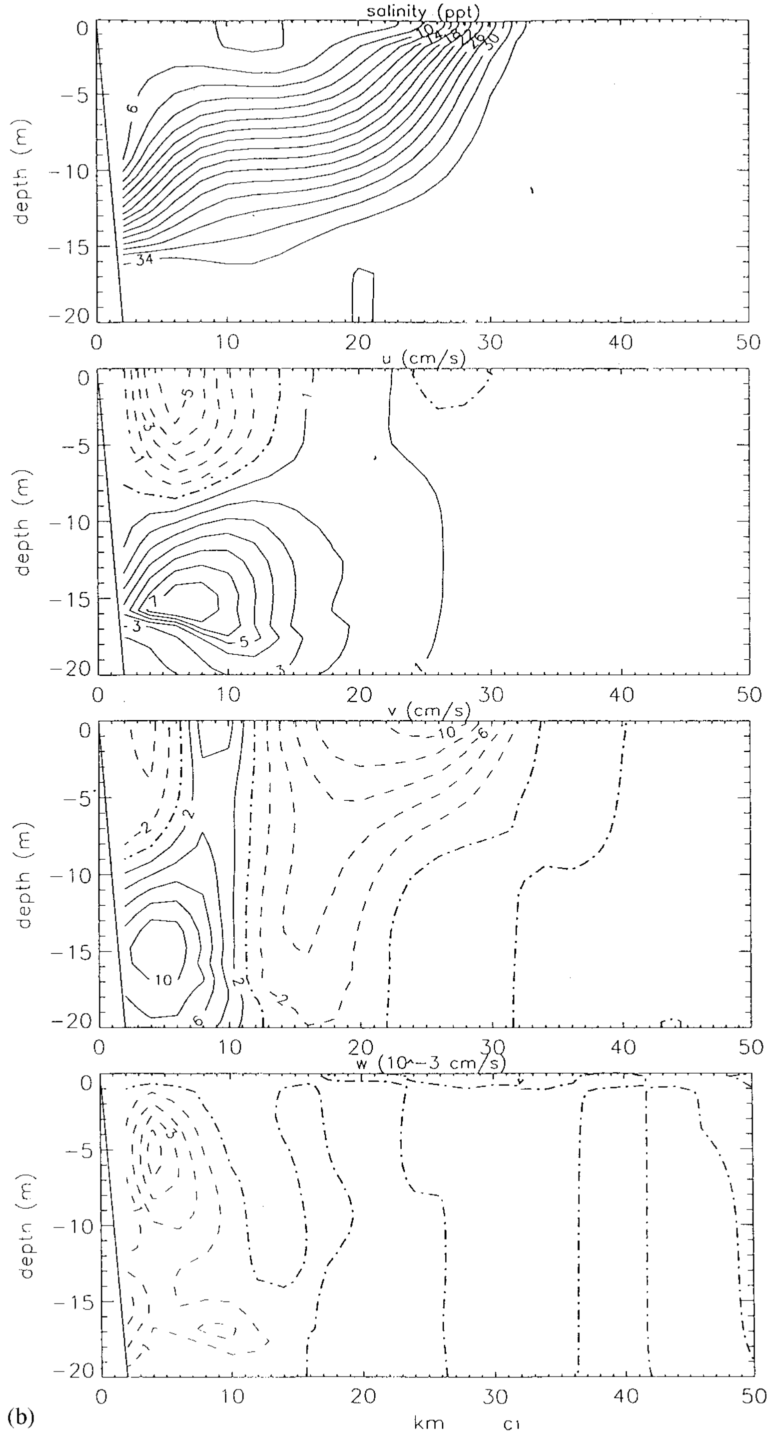

Figure 3 (*Continued*)

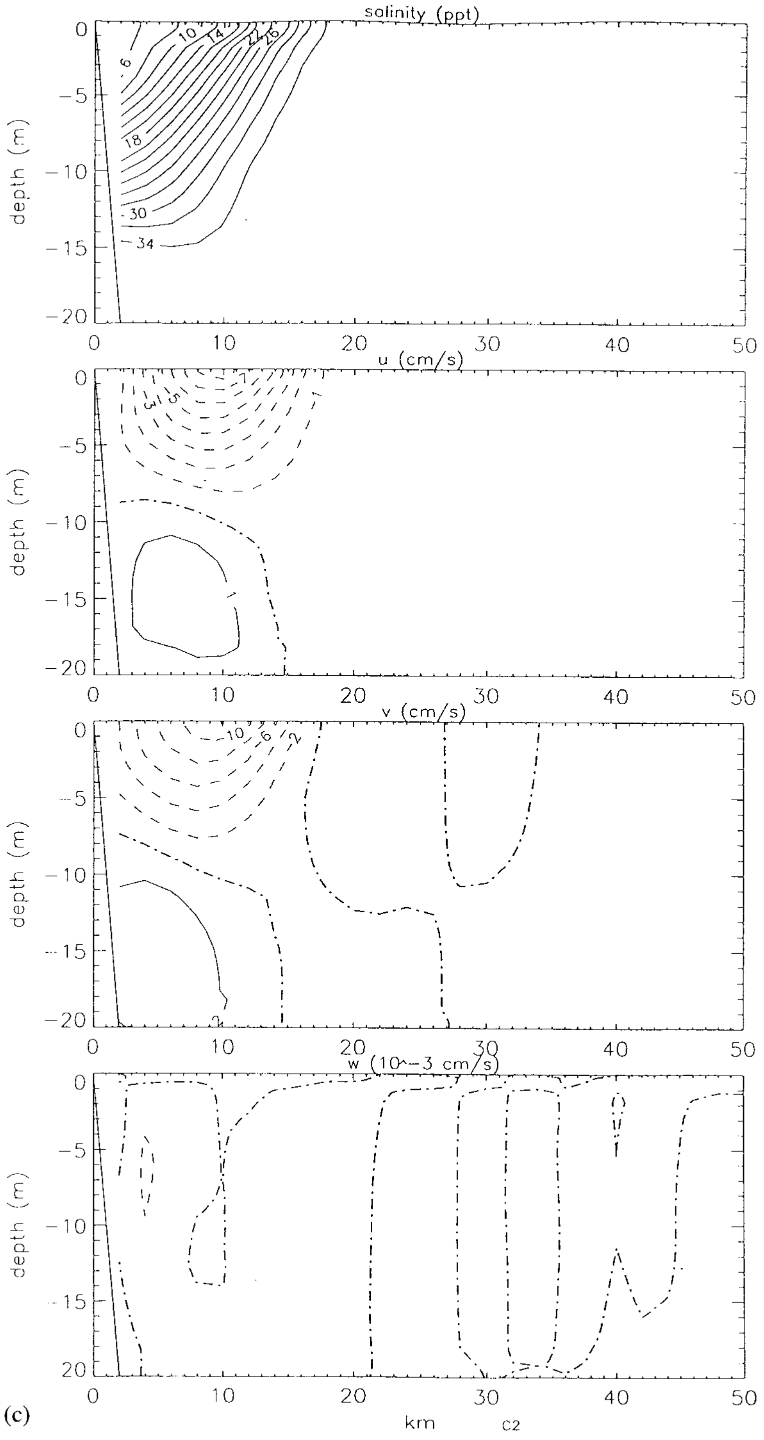

Figure 3 (*Continued*)

The spatial distribution of salinity contours at cross-section C_2 (Figure 3(c)) shows that the plume front (denoted by the 34 ppt contour) has moved significantly further off shore than previously with the plume confined to the surface layer (cf. Figure 3(c) and Figure 2(c)). Although the u and v components of current show similar distributions to those found in calculation 1, there are slight differences, with the vertical component of velocity being near zero. Values of viscosity and diffusivity were again smaller along this cross-section than those found in calculation 1.

The comparison of u and v velocity components computed with the two different turbulence energy models shows that although the choice of turbulence energy model only has a small effect upon the velocity field and values of the mixing coefficients, this does have a significant impact upon the thickness of the surface plume in the near coastal region and its southerly spread. Although the parameterization of mixing using turbulence closure models is more fundamental than the use of eddy coefficients, it is difficult to appreciate the roles of eddy viscosity and eddy diffusivity in determining the dynamics of the plume. To gain more insight into the relative importance and differences they produce in the spreading of the plume, in the next sections the authors consider a series of calculations in which the vertical mixing processes are parameterized using fixed coefficients.

3.4. Flat bottom $h = 20$ m, with A_v and K_v fixed at $A_v = 0.001$ m^2 s^{-1}, $K_v = 0.0001$ m^2 s^{-1} (calculation 3)

In the first calculation with fixed A_v and K_v (the turbulence energy models were not involved in any of these calculations), values of $A_v = 0.001$ m^2 s^{-1} and $K_v = 0.0001$ m^2 s^{-1} (calculation 3, Table I) were used throughout the whole region. These values are significantly larger, particularly the A_v value, from those found with the turbulence energy model. All other parameters were identical to those used previously.

Surface salinity contours (Figure 4(a)i) and current distributions, show that the plume front has moved a significantly shorter distance to the south than in the previous calculations, although the plume has spread slightly further north. The off-shore spread of the plume in the region of the discharge point is significantly less than that found previously (cf. Figure 4(a)i with Figure 3(a)i and Figure 2(a)i) with a second bulge having a larger off-shore extent to the south of the first one. The plume has now changed from supercritical to subcritical due to the change in mixing coefficients. The presence of this second bulge is primarily due to the fact that the southerly movement of the front is inhibited presumably by viscous effects that cause the fresh water to move off shore behind the front of the plume.

Salinity contours along cross-section C_1, show that the plume is not surface trapped, but extends to the sea bed with the salinity contours in the near bed region appearing to be nearly vertical. The resulting horizontal pressure gradient opposes the off-shore movement of the plume with the u component of velocity along this cross-section being near zero (Figure 4(b)). Contours of the v velocity show a significant southerly flow in the surface layer, with a northerly flow of more saline water at depth. The spatial distribution of the v component of velocity is significantly different from that found previously (Figure 2(b)), and to first-order can be regarded as a two layered flow field extending out to 20 km from the shore, rather than the southerly flow throughout the water column between 10 and 20 km that occurred in calculation 1 (Figure 2(b)).

3.5. *Flat bottom $h = 20$ m, with A_v and K_v fixed at $A_v = 0.001\ m^2\,s^{-1}$, $K_v = 0.0005\ m^2\,s^{-1}$ (calculation 4)*

To examine the extent to which K_v influences the solution, the previous calculation was repeated with K_v increased to 0.0005 $m^2\,s^{-1}$ (Table I, calculation 4). Surface salinity contours (Figure 5(a)), show a similar two bulge distribution to that found previously (calculation 3), although the off-shore spread of the plume in the region of the discharge point is significantly reduced (cf. Figure 5(a) and Figure 4(a)). Also, the southerly extent of the plume is approximately 20 km less than that found in calculation 3, although its off-shore extent away from the discharge point is increased.

The effect of increasing the vertical diffusion coefficient is to enhance the vertical mixing close to the discharge point (cf. Figure 5(b) and Figure 4(b)). Consequently, the low salinity surface water is mixed through the vertical before it can be advected off shore, producing the more vertical distribution of salinity contours that is evident in Figure 5(b) compared with Figure 4(b). The resulting intensified horizontal pressure gradient, together with the inertial effect of trying to move a larger mass of water off shore, appears to be the main reasons that prevent the off-shore spread of the plume close to the discharge point. The strong pressure

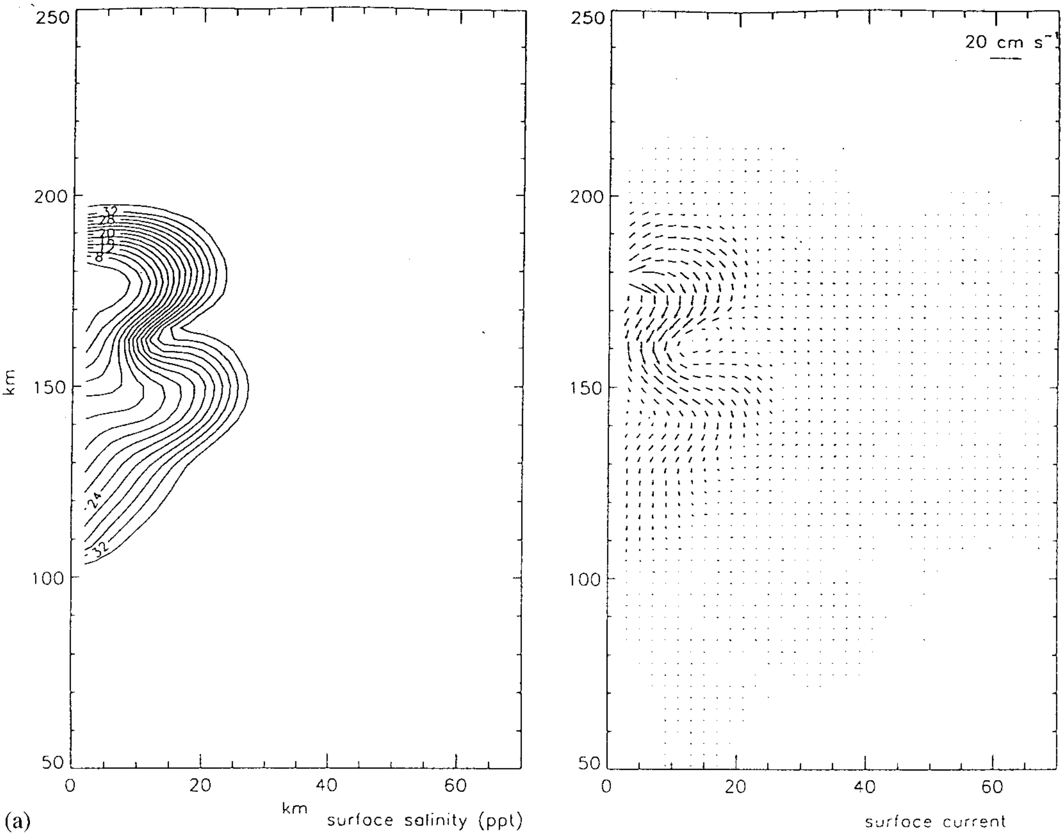

Figure 4. (a) Horizontal spatial distribution of surface salinity contours (ppt) and surface currents in a subdomain of the model, 15 days after the discharge of the plume computed with $A_v = 0.001$ $m^2\,s^{-1}$ and $K_v = 0.0001$ $m^2\,s^{-1}$ (calculation 3, Table I). (b) Contours after 15 days of salinity (ppt), u and v components of velocity ($cm\,s^{-1}$) at cross-section C_1 from calculation 3, Table I.

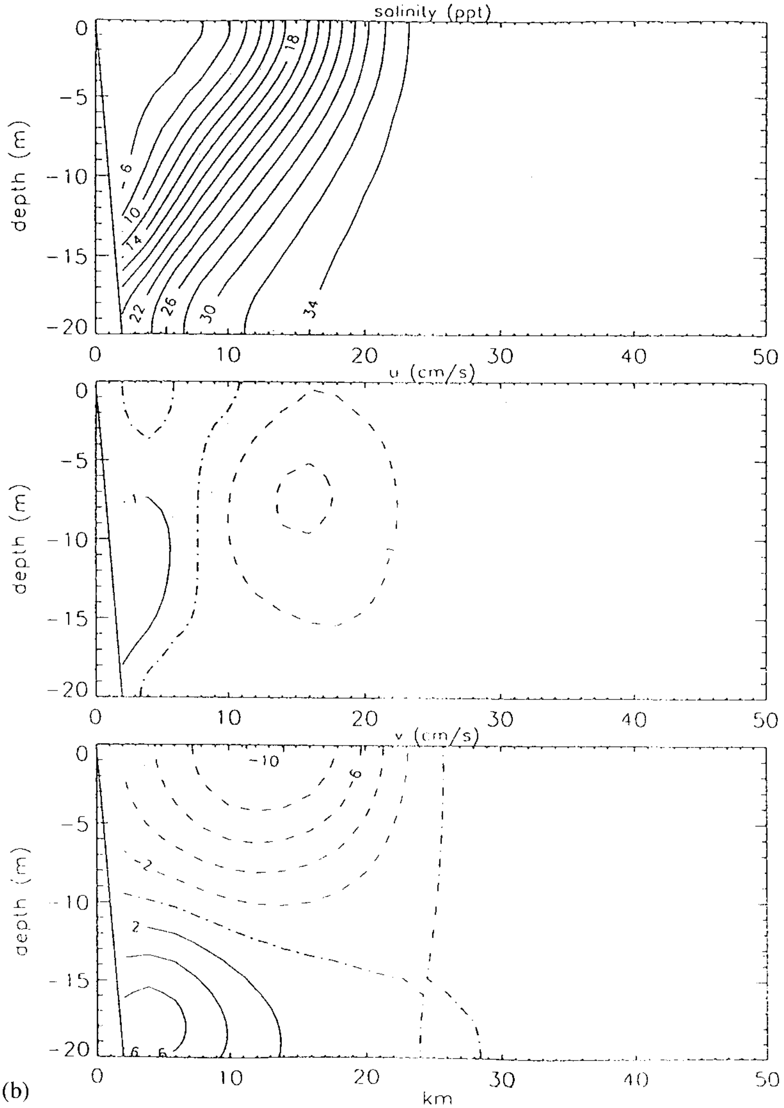

Figure 4 (*Continued*)

gradient associated with the sharp horizontal density gradient, gives rise to an intense near shore southerly flow in the surface layer where velocities are approximately twice those found in the previous calculation (cf. Figure 5(b) and Figure 4(b)). Below this surface layer there is a return northerly flow of comparable magnitude, although of smaller lateral spatial extent to that found previously. The strong southerly flow of fresh water, and the associated strong horizontal gradient of density gives rise to the baroclinic instability in the off-shore density contours that are evident at about 150 km from the southern end of the domain.

3.6. *Flat bottom $h = 20$ m, with A_v fixed at $A_v = 0.005$ m^2 s^{-1}*

3.6.1. $K_v = 0.0001$ m^2 s^{-1} (calculation 5). To examine the influence of increasing A_v with K_v fixed at 0.0001 m^2 s^{-1}, calculation 3 was repeated with A_v increased to 0.005 m^2 s^{-1} (calculation 5, Table I). Contours of surface salinity (Figure 6(a)) show that the maximum off-shore extent occurs in the region of the discharge point with a nearly uniform northerly and southerly spread of the plume that has a distribution similar to that found when rotational effects are neglected.

The uniform spreading of the plume and the absence of any sign of instability along the plume front compared with calculation 3 (Figure 4(a)) suggest that the increased value of A_v has reduced current shear in the vertical and in the horizontal and hence the onset of instability. Although salinity contours along cross-section C_1, show comparable mixing with that found in calculation 3 (cf. Figure 6(b) and Figure 4(b)) where the same K_v value was used, there is a significant reduction in the vertical shear in the v component of velocity (cf. Figure 6(b) and 4(b)), due to the increased A_v value.

3.6.2. $K_v = 0.0005$ m^2 s^{-1} (calculation 5R). In a repeat of calculation 5, namely calculation 5R, Table I, A_v was maintained at 0.005 m^2 s^{-1}, but K_v was increased to 0.0005 m^2 s^{-1} to represent enhanced vertical diffusion possibly due to wind turbulence in the near coastal

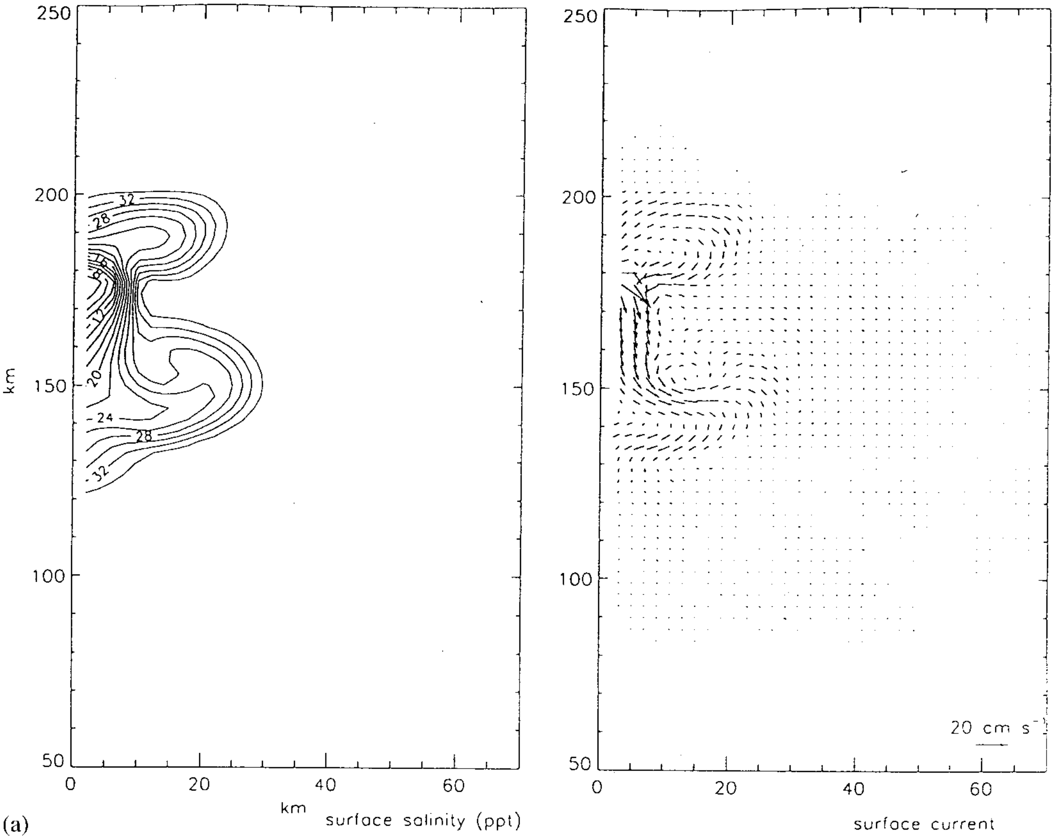

Figure 5. (a) As Figure 4(a) but computed with $A_v = 0.001$ m^2 s^{-1} and $K_v = 0.0005$ m^2 s^{-1} (calculation 4, Table I). (b) As Figure 4(b) but computed with $A_v = 0.001$ m^2 s^{-1} and $K_v = 0.0005$ m^2 s^{-1} (calculation 4, Table I).

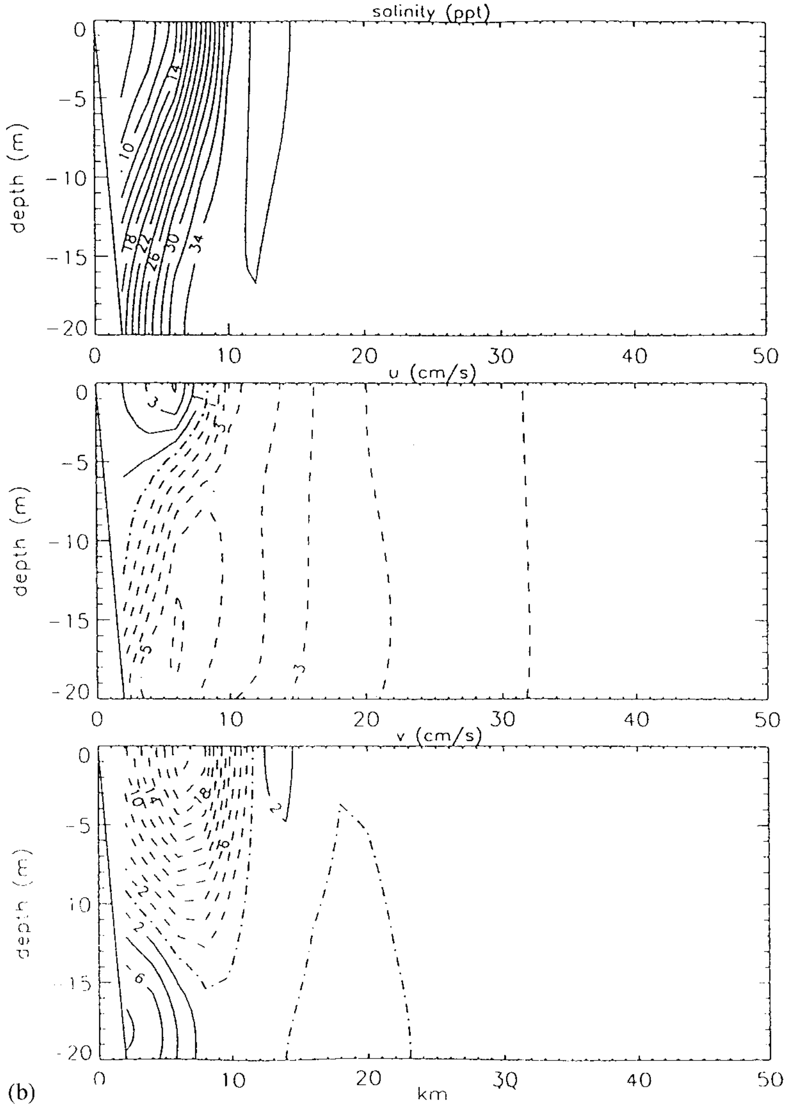

Figure 5 (*Continued*)

region. The effect of increasing the vertical diffusion is to significantly reduce the spread of the plume (cf. Figure 6(c) with (a)) although surface currents were comparable with those found previously (cf. Figure 6(c) and (a)). Comparing salinity contours (Figure 6(d)) with those found previously, shows that the vertical mixing in the region of the discharge has been significantly increased, and this together with the high value of A_v has reduced the off-shore and along-shore components of velocity. The along-shore velocity has been reduced by a factor of ten below that found in calculation 4 ($K_v = 0.0005$ m^2 s^{-1}, $A_v = 0.001$ m^2 s^{-1}) suggesting that when the vertical diffusion coefficient K_v is large, then an increase in A_v significantly reduces the magnitude of the along-shore flow and hence the spread of the plume.

These calculations suggest that the spread of the plume is not related in a simple manner to either A_v or K_v, but the nature of its spreading is rather complex, although increasing A_v and K_v reduces the spread and the influence of rotational effects upon the off-shore extent of the plume. In essence, increasing K_v enhances vertical mixing, reducing the spread of the plume, and gives rise to a more uniform distribution of salinity in the region of the discharge point. The tendency for instability along the plume front is reduced. An increase in A_v reduces vertical shear, which leads to a reduced surface current and plume spreading with an associated reduction in frontal instability.

4. CALCULATIONS WITH DEPTH INCREASING OFF SHORE

4.1. Depth varying, A_v and K_v computed with the 1-eqn tke model (calculation 6)

In the previous series of calculations, the water depth was constant at $h = 20$ m. In this section, a series of calculations is described, initially using the one-equation turbulence energy

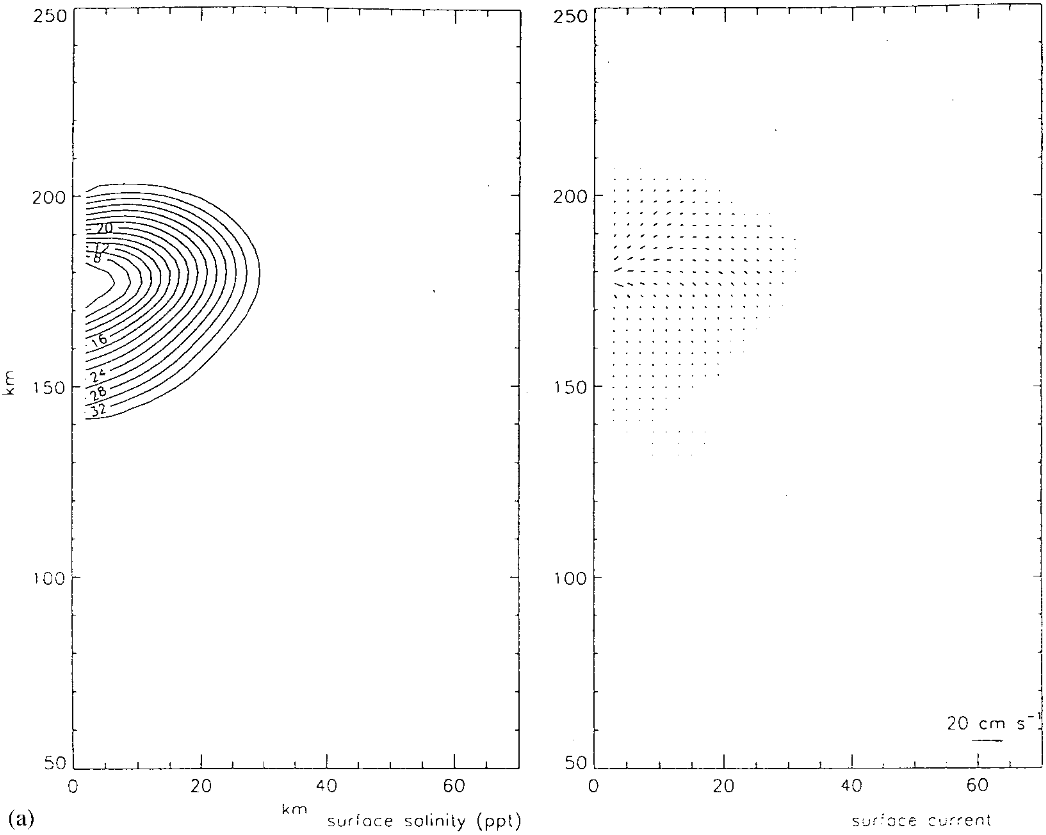

(a)

Figure 6. (a) Horizontal spatial distribution of salinity contours (ppt) and surface currents in a subdomain of the model, 15 days after the discharge of the fresh water plume computed with $A_v = 0.005$ m^2 s^{-1} and $K_v = 0.0001$ m^2 s^{-1} (calculation 5, Table I). (b) As Figure 4(b) but computed with $A_v = 0.005$ m^2 s^{-1} and $K_v = 0.0001$ m^2 s^{-1} (calculation 5, Table I). (c) As Figure 4(a) but computed with $A_v = 0.005$ m^2 s^{-1} and $K_v = 0.0005$ m^2 s^{-1} (calculation 5R, Table I). (d) As Figure 4(b) but computed with $A_v = 0.005$ m^2 s^{-1} and $K_v = 0.0005$ m^2 s^{-1} (calculation 5R, Table I).

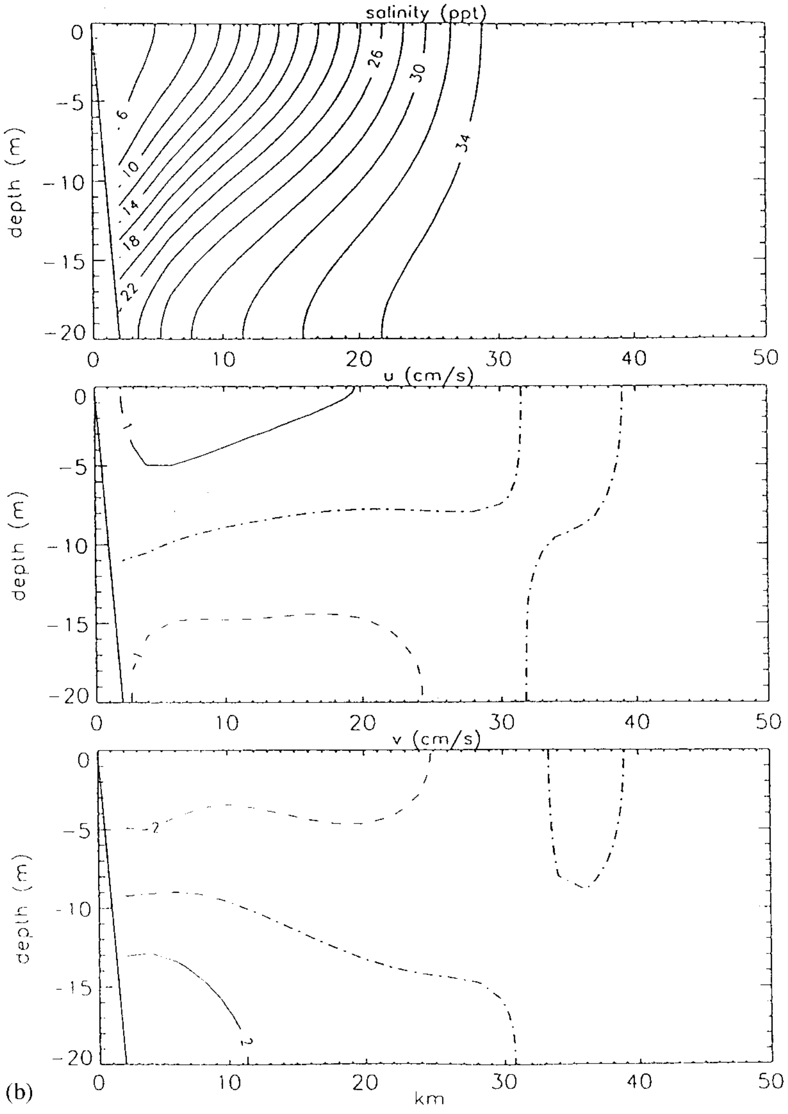

Figure 6 (*Continued*)

closure model (calculation 6, Table I) in which the near shore topography changes. A water depth that increases linearly from 20 m in the nearest coastal grid box to 110 m at approximately 48 km off shore was used, in order to examine the influence of near coastal topography upon the spread of the Ebro plume.

Surface salinity contours and current vectors (Figure 7(a)) at day 15 show that the maximum extent of the off-shore spread of the plume in the vicinity of the out flow has been reduced compared with the flat bottom case (Figure 2(a)), with the downstream extent of the plume being increased by approximately 20 km. In the sloping bottom case, the wave-like perturbations of the off-shore extent of the plume are smaller, with the secondary off-shore displacement of comparable magnitude with the first and occurring much closer to it, namely at 160

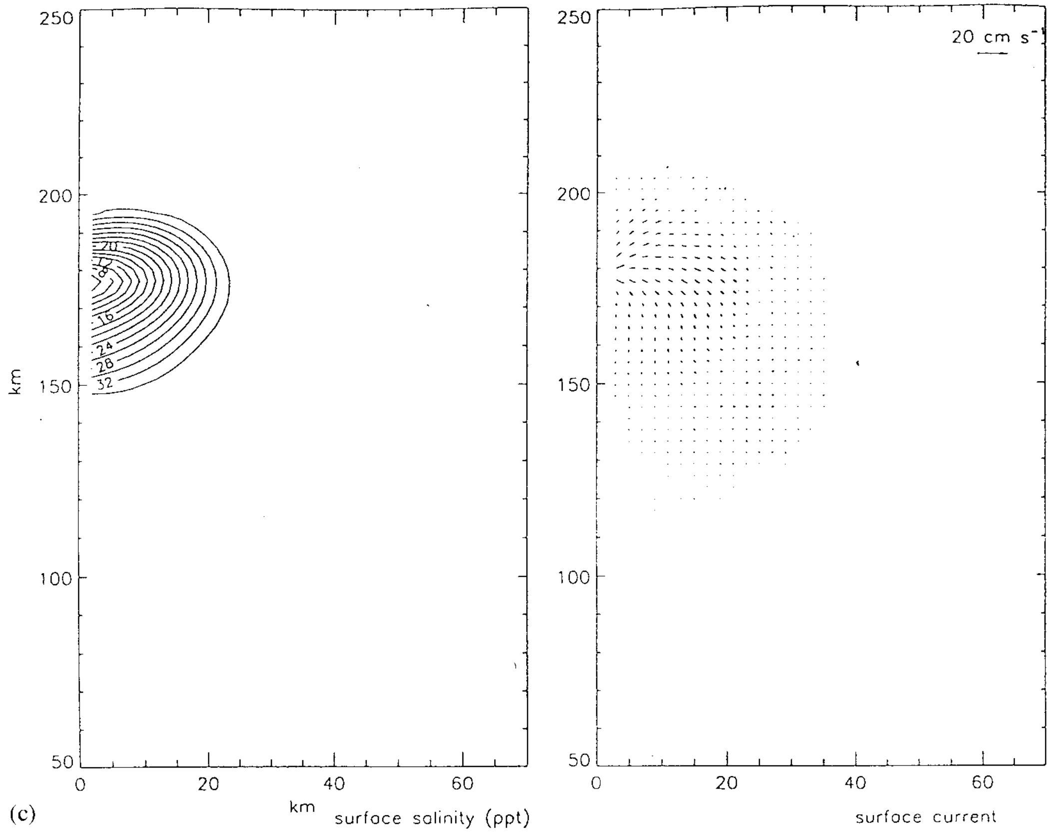

Figure 6 (*Continued*)

km rather than 130 km as found in calculation 1. These differences in the spatial distribution of the surface salinity contours are reflected in the surface currents and those at depth, with surface currents in the present calculation exhibiting a small gyre at the location of the secondary maximum, which was not found in the previous calculation. In the case of a sloping bottom, conservation of vorticity constrains the off-shore movement of the plume producing a narrower coastal trapped jet (cf. Figure 7(a) and Figure 2(a)).

It is apparent from a comparison of the cross-sectional plots along C_1 (cf. Figure 7(b) and Figure 2(b)), that in the sloping bottom case, the plume front intersects the sea bed significantly closer to the coastline than in the previous case. Also, vertical mixing has been reduced with vertical density gradients in the off-shore region being significantly stronger than in the flat bottom case. The reason for this is that in the sloping bottom case as we move further off shore, the region of enhanced bed mixing moves further away from the surface layer and hence the effect of bed generated mixing upon the plume is reduced (cf. Figure 7(b) and Figure 2(b)). Regions of enhanced mixing are clearly evident in both cases in the near shore area and the bottom boundary layer where turbulence energy and eddy viscosity and diffusivity (not shown) exceed their background values and this is responsible for the well-mixed regions that are evident in Figure 7(b).

Contours of the *u* component of velocity show the characteristic on shore flow in the surface layer that occurs just to the south of the discharge point (Figure 7(b)), although the position

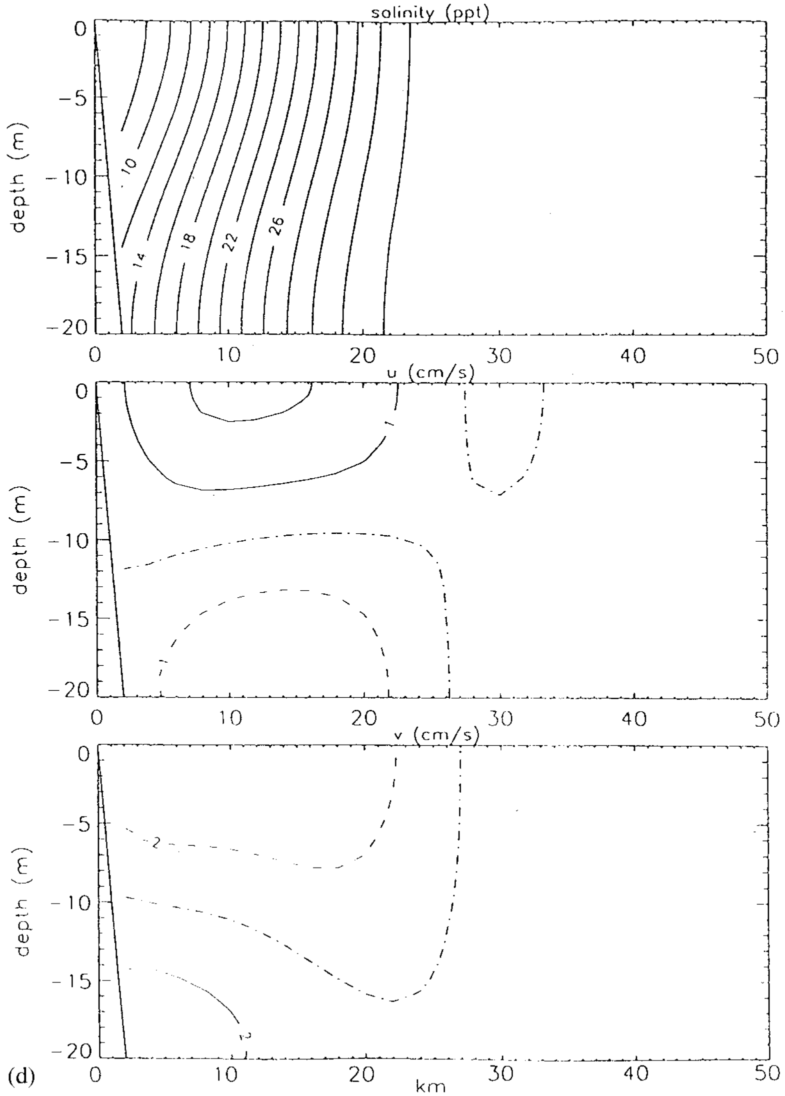

Figure 6 (*Continued*)

of the maximum on-shore flow has been moved further off shore (cf. Figure 7(b) and Figure 2(b)), and the region of off-shore flow at depth has been reduced. Although contours of the v component of velocity, exhibit similar spatial distributions to those found in the flat bottom calculation (cf. Figure 7(b) and Figure 2(b)), the region of significant southerly flow (taken as the area where the currents exceed 2 cm s^{-1}) is confined to the upper 15 m of the flow rather than extending to the sea bed as in the flat bottom case. A northerly return flow at the bed, with currents exceeding 10 cm s^{-1} (comparable with that in the flat bottom case) is evident in Figure 7(b).

Contours of the vertical velocity show a downwelling in the near shore region (up to 12 km from the coast) within approximately the upper 20 m of the water column. The magnitude of this downwelling and its off-shore extent are comparable with that found in the flat bottom case, although with a sloping bottom a near bed region of up-welling is evident below 20 m, arising due to the on-shore flow in the near bed region, which is evident in the *u* component of velocity (Figure 7(b)), which did not occur in the flat bottom case.

Cross-sectional plots of salinity and velocity (Figure 7(c)) along cross-section C_2, show that the plume front (denoted by the 34 ppt contour) extends from sea surface to sea bed with the front of the plume at the surface having moved about 15 km off shore compared with Figure 2(c) in which the plume was more well-mixed in the vertical and had only propagated about 10 km off shore. The increased vertical mixing found in the flat bottom case leads to an increase in vertical eddy viscosity producing a viscous bottom boundary layer, which in the shallower water depths influences the surface layer.

The reduction in the downstream distribution of current meanders when an off-shore slope is introduced (cf. Figure 7(a) and Figure 2(a)) means that the cross-shelf distribution of the *u* component of velocity at cross-section C_2 reaches near zero (Figure 7(c)) compared with the flat bottom case (Figure 2(c)) with the flow in essence aligned with the shoreline in the sloping bottom case, to the south of this point.

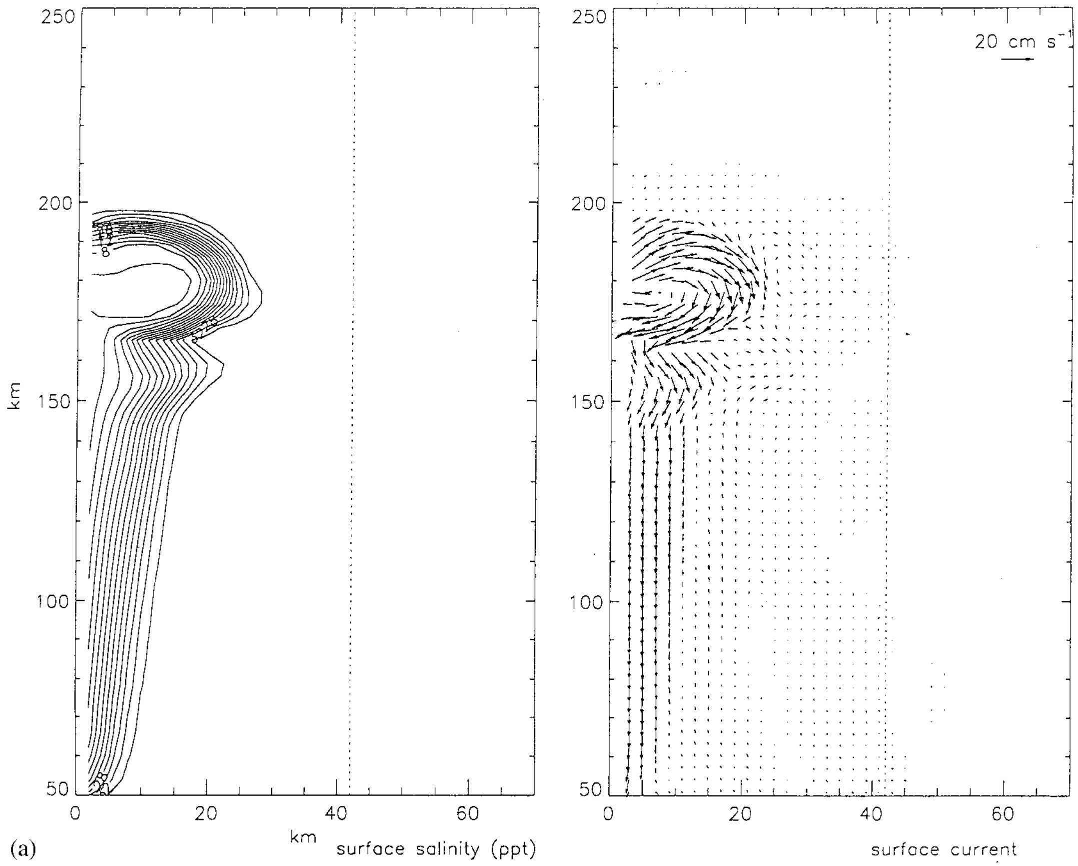

Figure 7. (a) As Figure 6(a) but for a sloping bottom topography (with $h = 20$ m at the coast) and the one-equation turbulence energy model (calculation 6, Table I). (b) Contours after 15 days of salinity (ppt) *u*, *v* and *w* ($\times 10^{-3}$) components of velocity (cm s^{-1}), turbulent kinetic energy ($\log_{10}$, $m^2 s^{-2}$) and viscosity ($\log_{10}$, $m^2 s^{-1}$) at cross-section C_1 computed with the one-equation turbulence energy model and a sloping bottom (calculation 6, Table I). (c) As (b) but at cross-section C_2, and no vertical velocity (calculation 6, Table I).

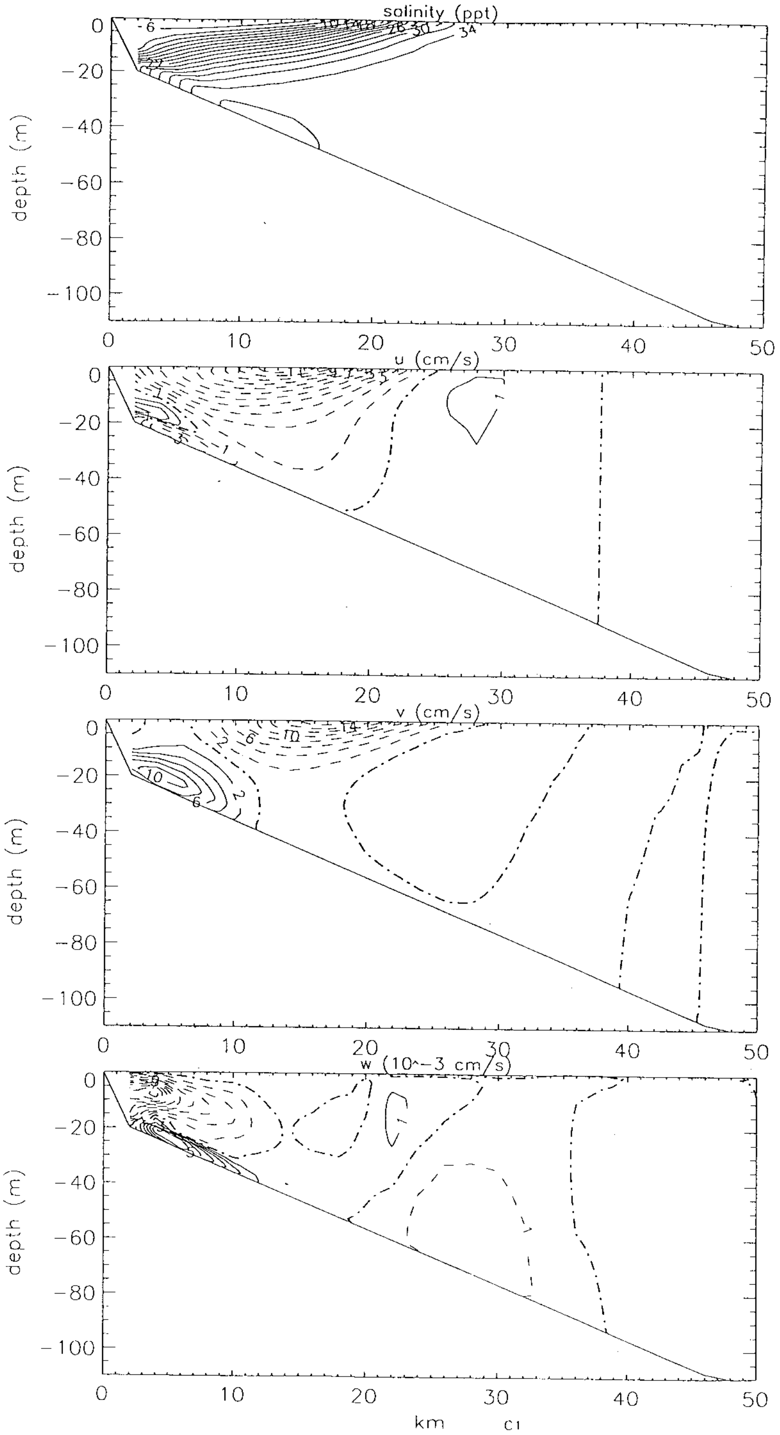

Figure 7 (*Continued*)

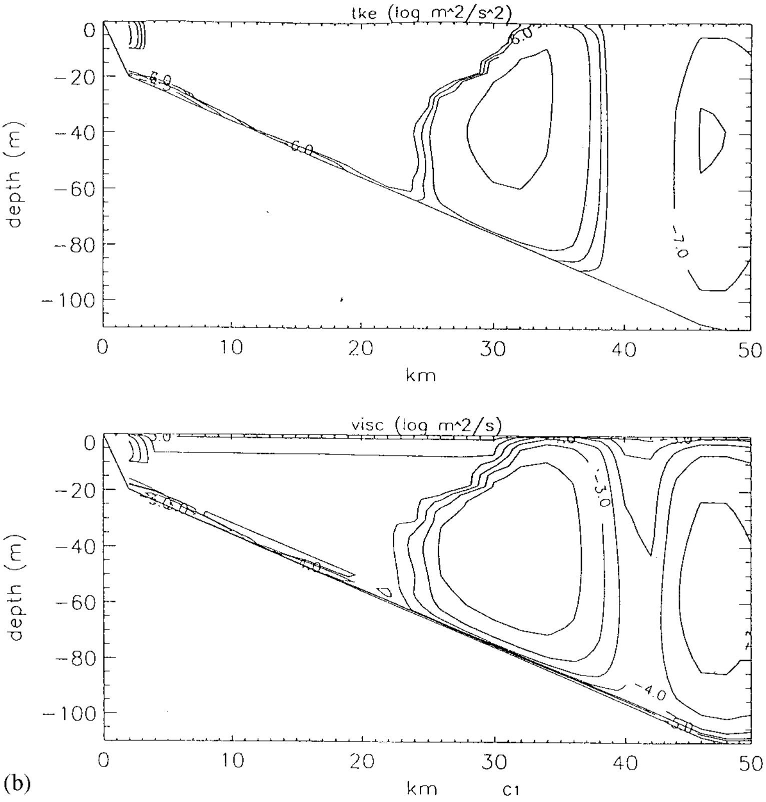

(b)

Figure 7 (*Continued*)

Contours of the v component of velocity (Figure 7(c)) show similar spatial distributions to those found in the flat bottom case although the region of southerly surface flow has extended further off shore (cf. Figure 7(c) and Figure 2(c)).

4.2. *Depth varying, A_v and K_v fixed at $A_v = 0.001\ m^2\ s^{-1}$, $K_v = 0.0001\ m^2\ s^{-1}$ (calculation 7)*

In the previous calculations the coefficients of vertical diffusion of momentum (A_v) and density (K_v) were computed using the turbulence energy closure model, in which these terms evolved with space and time. In order to understand the role of A_v and K_v in determining the dynamics of the spreading of the Ebro plume, in the case of more realistic topography, a number of calculations were performed in which constant values were assigned to these parameters.

Initially (calculation 7, Table I) $A_v = 0.001$ m^2 s^{-1}, with $K_v = 0.0001$ m^2 s^{-1}, and an identical sloping sea bed topography was used to that in calculation 6. Contours of surface salinity (Figure 8(a)) show that the surface southerly spread of the plume has been significantly reduced (cf. Figure 8(a) and Figure 7(a)) by this value of vertical diffusion, which is significantly larger than that found with the turbulence energy model. The principal effect of this increase in vertical diffusion is to entrain more saline water from below, which leads to an increase in the thickness of the surface layer (cf. Figure 8(b) and Figure 7(b)) with a resulting reduction in the currents in this layer (cf. Figure 8(b) and Figure 7(b)). The effect of the decrease in the flow of the surface layer is that the fresh water discharged into it can no longer

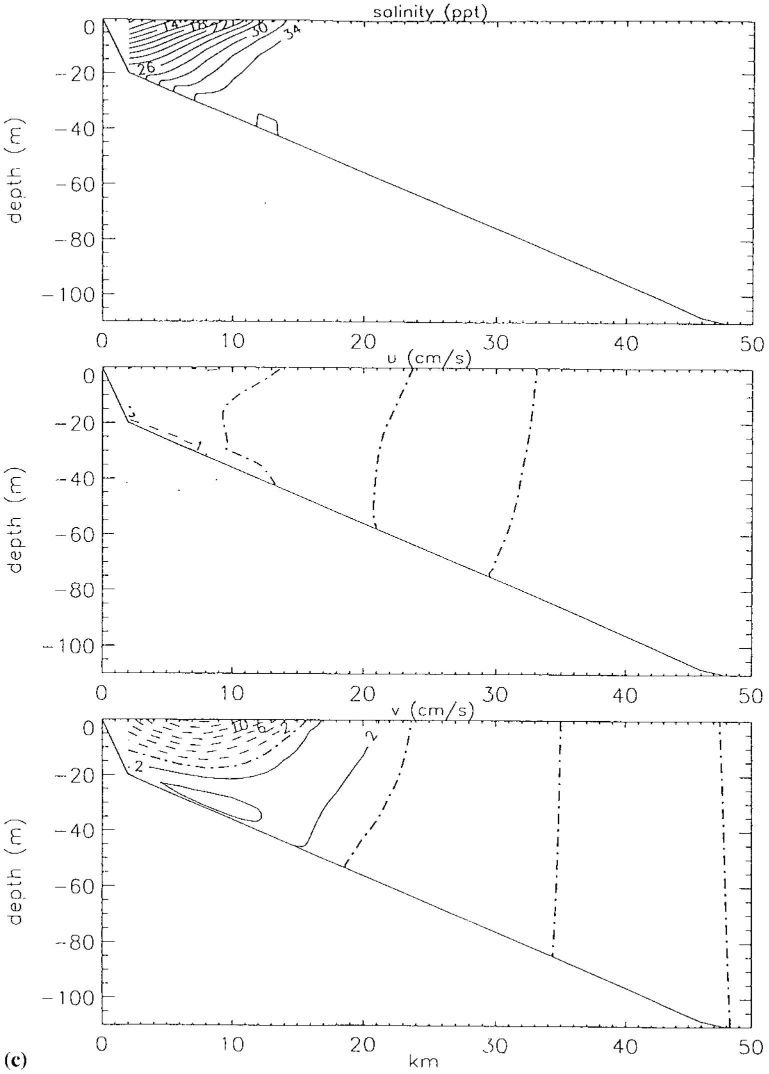

Figure 7 (*Continued*)

propagate as rapidly off shore or southward. Also, since the off-shore extent of the plume is constrained by conservation of vorticity due to the sloping bottom, the maximum off-shore spread of the surface plume is comparable with that found previously, with the fresh water discharge being accommodated by an increased northward spreading of the plume, and a wider plume to the south of the discharge point (cf. Figure 8(a) and Figure 7(a)). This is consistent with the results of the flat bottom calculations. Although this comparison with the turbulence energy model appears to confirm the conclusions reached previously in the flat bottom case, the role of K_v independently of A_v cannot be clearly identified in the case of the turbulence model, since both K_v and A_v vary with horizontal position and time in a complex manner. For this reason a further calculation was performed with A_v fixed at its previous value and K_v increased.

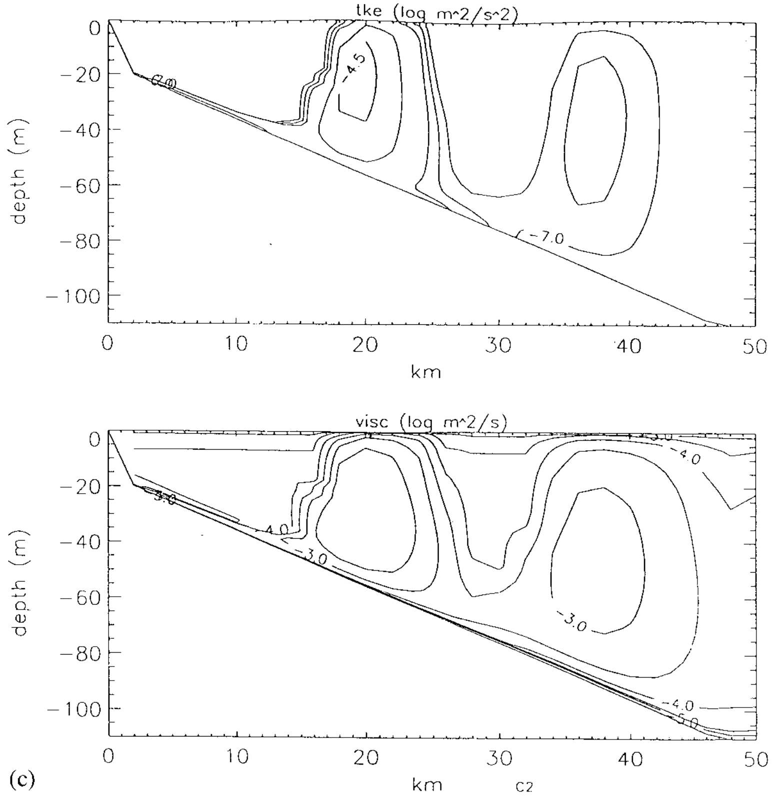

Figure 7 (*Continued*)

4.3. Depth varying, A_v and K_v fixed at $A_v = 0.001\ m^2\,s^{-1}$, $K_v = 0.001\ m^2\,s^{-1}$ (calculation 8)

Repeating the calculation (calculation 8, Table I) with $K_v = 0.001$ m^2 s^{-1} (a tenfold increase in the value used previously) leads to a reduced off-shore spreading of the plume with the 34 ppt contour only extending about 15 km off shore (Figure 9(a)) compared with previously where it extended 25 km off shore (Figure 8(a)) giving rise to an intensification of surface current in a narrow near shore band (Figure 9(a)).

The reduced off-shore and southerly spreading of the plume increases the northerly spreading (cf. Figure 9(a) and Figure 8(a)) in an analogous manner to that found in the flat bottom case (calculation 4), although the tendency for instability effects to occur along the plume front is reduced (cf. Figure 9(a) and Figure 5(a)), due to the vorticity constraint arising from the bottom slope.

This increase in K_v values enhances the vertical mixing close to the discharge point and reduces the off-shore spreading of the plume front, as the lighter water mixes to a greater depth (cf. Figure 8(b) and Figure 9(b)). This reduction in the off-shore spread of the plume, enhances the local horizontal density gradient, producing a stronger v component of velocity within a narrower near shore region than that found previously (cf. Figure 9(b) and Figure 8(b)), and is also evident in the surface distribution (Figure 9(a) and Figure 8(a)).

To examine if features like the onset of instability can occur in the case of a sloping bottom, and determine the value to which K_v has to be reduced to produce such effects a further calculation was performed.

4.4. Depth varying, A_v and K_v fixed at $A_v = 0.001\ m^2 s^{-1}$, $K_v = 0.00001\ m^2 s^{-1}$ (calculation 9)

In a subsequent calculation (calculation 9, Table I), K_v was reduced by a factor of ten below that used in calculation 7. This reduction in K_v lead to an enhanced off-shore spreading of the plume (cf. Figure 10(a) and Figure 8(a)), although the northward and southward extent of the plume were comparable with that found in calculation 7, with the plume front showing an increased tendency to exhibit a 'wave-like' pattern in both salinity contours and surface currents (Figure 10(a)) due to the onset of frontal instability. The reduction in K_v decreases the vertical mixing of the fresh water discharge, with salinity contours at cross-section C_1 (Figure 10(b)), showing a much greater surface spreading and reduced vertical mixing than found previously (Figure 8(a)). This reduction in vertical mixing means that although the fresh water has extended further off shore than previously, this spreading is confined to a thinner surface layer. Consequently, for a given volume discharge the same northward and southward spread found previously can occur.

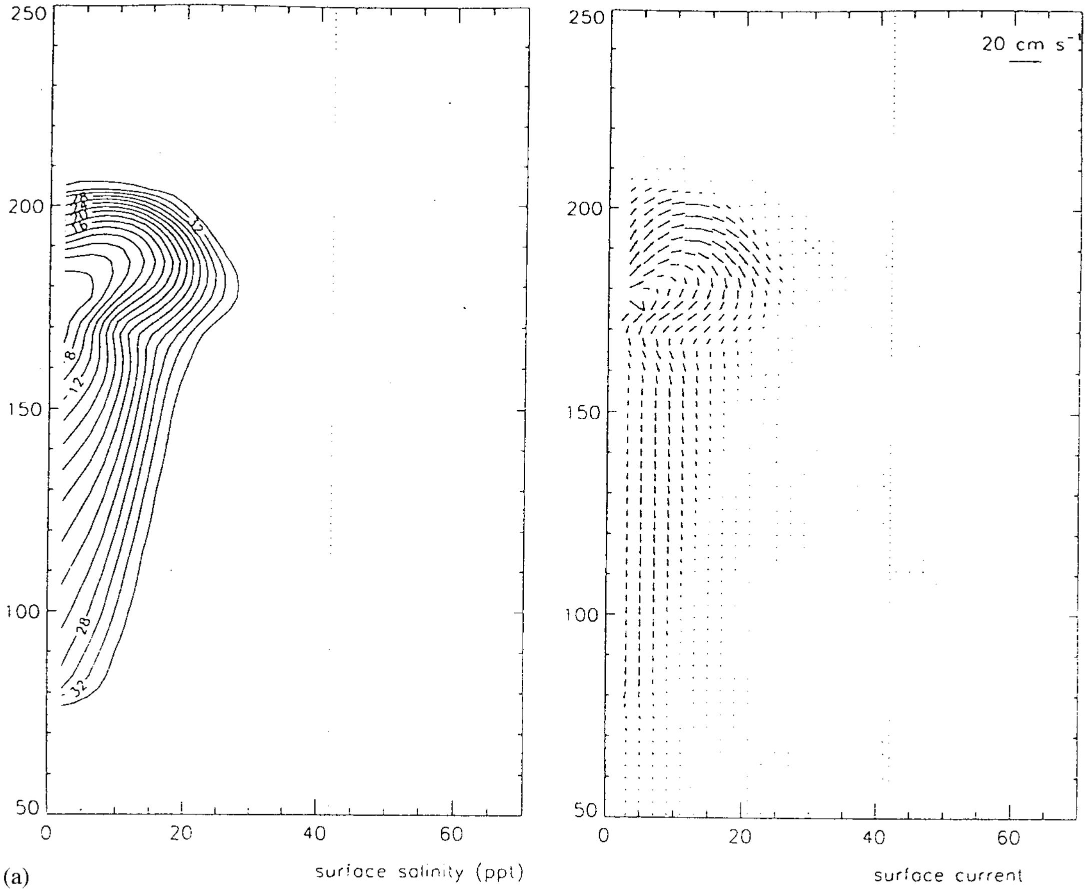

Figure 8. (a) As Figure 7(a) but with $A_v = 0.001$ m^2 s^{-1} and $K_v = 0.0001$ m^2 s^{-1} (calculation 7, Table I). (b) Contours after 15 days of salinity (ppt), u and v components of velocity (cm s^{-1}) at cross-section C_1 computed with $A_v = 0.001$ m^2 s^{-1} and $K_v = 0.0001$ m^2 s^{-1} (calculation 7, Table I).

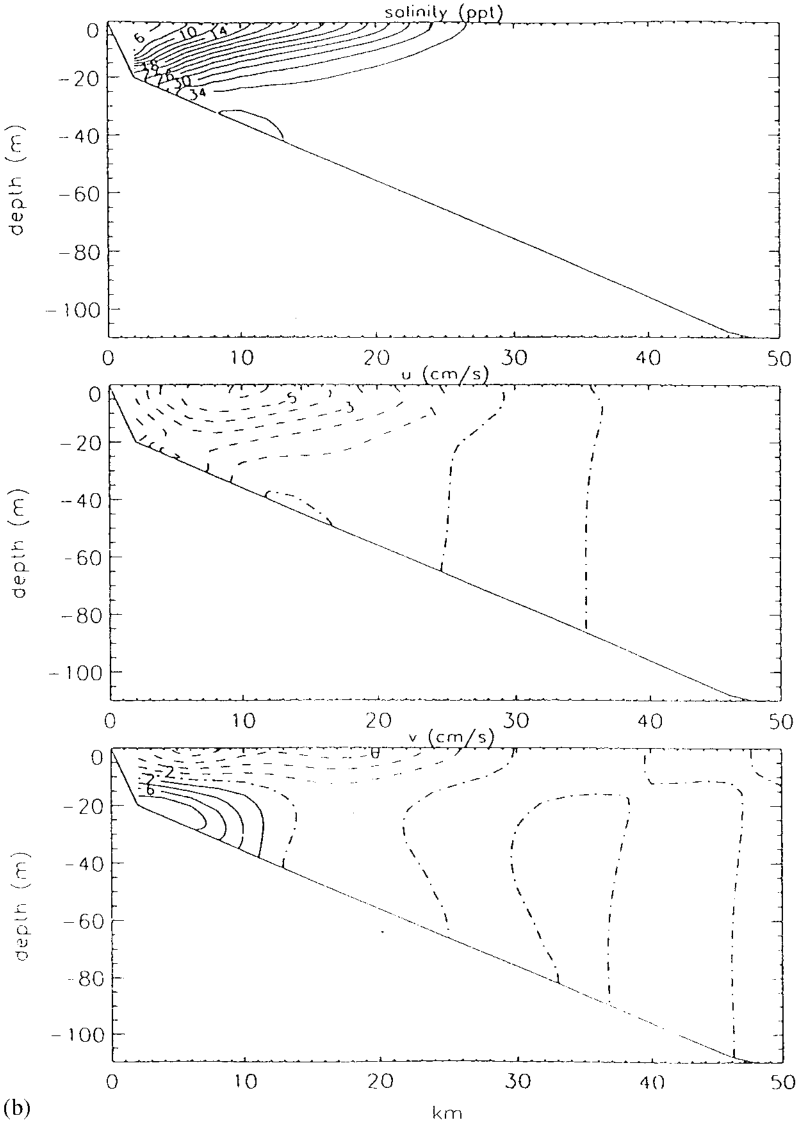

Figure 8 (*Continued*)

Although contours of the u component of velocity at cross-section C_1, show a reduction in velocity compared with that found previously, (cf. Figure 10(b) and Figure 8(b)) the maximum v component of surface flow is increased to a southward flow of over 10 cm s^{-1}, producing the significant increased spreading of the freshwater (taken as the 6 ppt contour) to the south found in this calculation (Figure 10(a)) compared with that obtained previously (Figure 8(a)). Similarly, in the near coastal bed region, the northward flow of more saline water to compensate for the southward flow of fresh water is increased (cf. Figure 10(b) and Figure 8(b)).

This series of calculations has shown that for a fixed A_v value, K_v is critical in determining the spread of the plume. As K_v is reduced, the off-shore spread of the plume increases, with the plume spreading as a surface layer due to the reduced vertical mixing. There is also an increased tendency towards frontal instability. Increasing K_v enhances vertical mixing, and the influence of topography appears to increase, reducing the off-shore spread of the plume. The increased vertical mixing reduces the southward spread of the plume, and consequently for a given discharge rate, the northward spread increases to accommodate the outflow from the river.

In a subsequent calculation, the authors investigate the role of A_v by maintaining a fixed K_v.

4.5. Depth varying, A_v and K_v fixed at $A_v = 0.0001\ m^2\,s^{-1}$, $K_v = 0.0001\ m^2\,s^{-1}$ (calculation 10)

In the next calculation (calculation 10, Table I), K_v was maintained at the same value as that used in calculation 7, but A_v was reduced by a factor of ten. Comparing Figure 11(a) and Figure 8(a) shows that the off-shore spread of the plume has been reduced by the decrease in A_v value with the southward extent of the plume being increased with no significant change in the northward spread of the plume. The decrease in the A_v value leads to a sharper horizontal density gradient near the plume front, and hence (as in the case of a decreased K_v value) to wave like features produced by frontal instability.

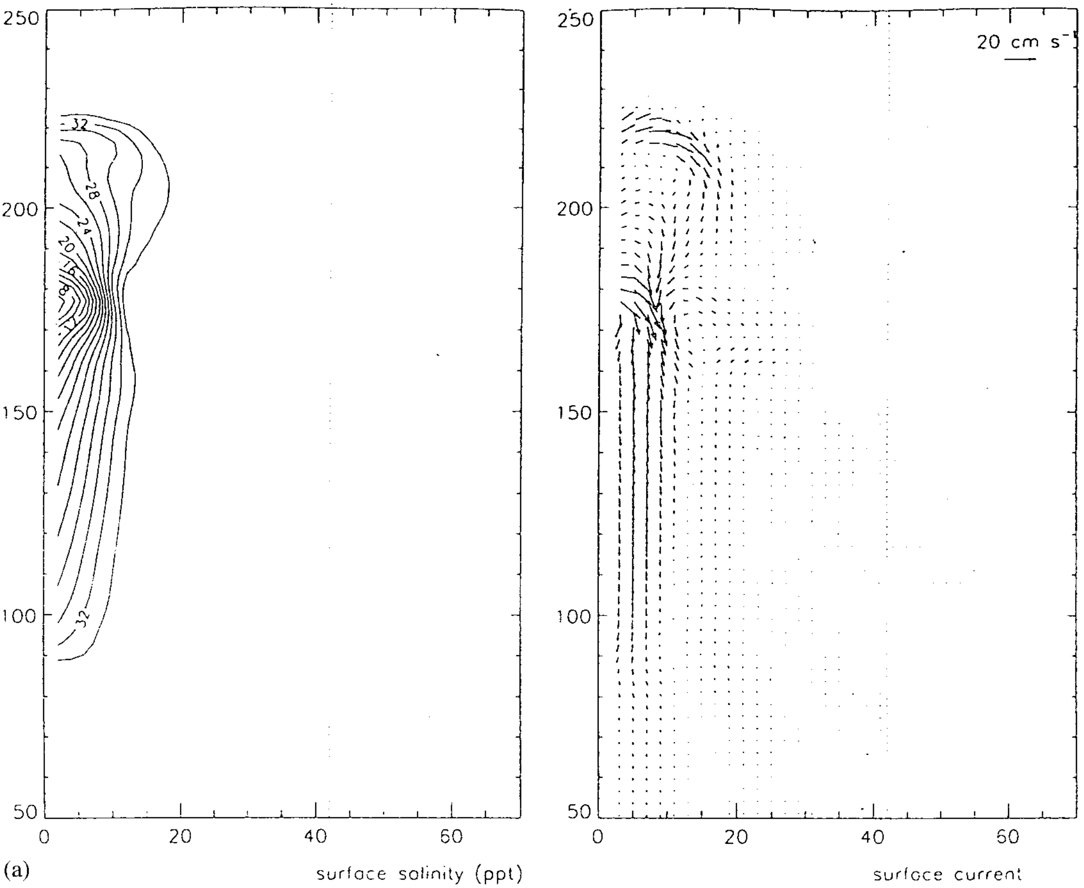

Figure 9. (a) As Figure 8(a) but with $A_v = 0.001$ m^2 s^{-1} and $K_v = 0.001$ m^2 s^{-1} (calculation 8, Table I). (b) As Figure 8(b) but with $A_v = 0.001$ m^2 s^{-1} and $K_v = 0.001$ m^2 s^{-1} (calculation 8, Table I).

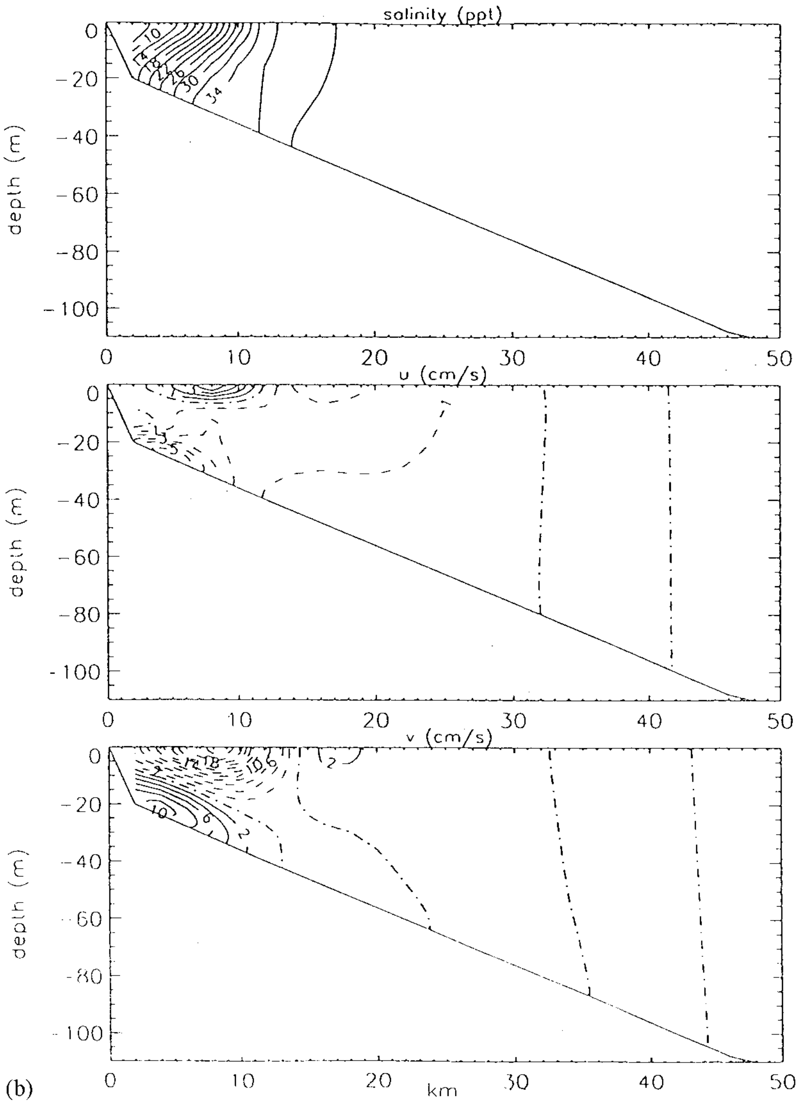

Figure 9 (*Continued*)

Salinity contours along cross-section C_1 are different from those found previously (calculation 7, Figure 8(b)) despite the fact that both models have the same K_v values. In particular, the off-shore spread has been reduced and hence the thickness of the surface layer has increased. The main reason for the reduced off-shore spread of the plume is that the on-shore flow in the surface layer along cross-section C_1 (cf. Figure 11(b) and Figure 8(b)) has been enhanced by the reduced A_v value. Similarly, the flow to the south in the near shore region, and the return flow at depth has been increased by reducing the A_v value (cf. Figure 11(b) and Figure 8(b)).

This calculation suggests that the effect of A_v upon the southward spread of the plume is similar to that found for K_v in that reducing A_v enhances the southward flow, and the tendency for increased frontal instability. However, K_v appears to have a greater effect than A_v. Also, the effect of A_v and K_v upon the off-shore spread of the plume in the depth varying case is different. The dominance of K_v upon the solution is confirmed by a further calculation in which A_v was maintained at 0.0001 $m^2 s^{-1}$, but K_v was increased to 0.001 $m^2 s^{-1}$.

4.6. Depth varying, A_v and K_v fixed at $A_v = 0.0001$ $m^2 s^{-1}$, $K_v = 0.001$ $m^2 s^{-1}$ (calculation 11)

Surface salinity contours computed with these values of A_v and K_v (calculation 11, Table I), show very similar spatial distributions (cf. Figure 12(a) and Figure 9(a)) to those computed with $A_v = 0.001$ $m^2 s^{-1}$ and $K_v = 0.001$ $m^2 s^{-1}$ (calculation 8, Table I), namely the significant spread of the plume to the north and the reduced off-shore spread in the region of the discharge. In essence, the solution with a fixed $K_v = 0.001$ $m^2 s^{-1}$ does not appear to be very sensitive to a reduction of A_v from 0.001 to 0.0001 $m^2 s^{-1}$. This is in marked contrast to the change found with a fixed $A_v = 0.001$ $m^2 s^{-1}$ when K_v was reduced from 0.001 to 0.0001 $m^2 s^{-1}$ (calculations 7 and 8) (cf. Figure 8(a) and Figure 9(a)) where the plume characteristics changed from supercritical (Figure 8(a)) to subcritical Figure 9(a).

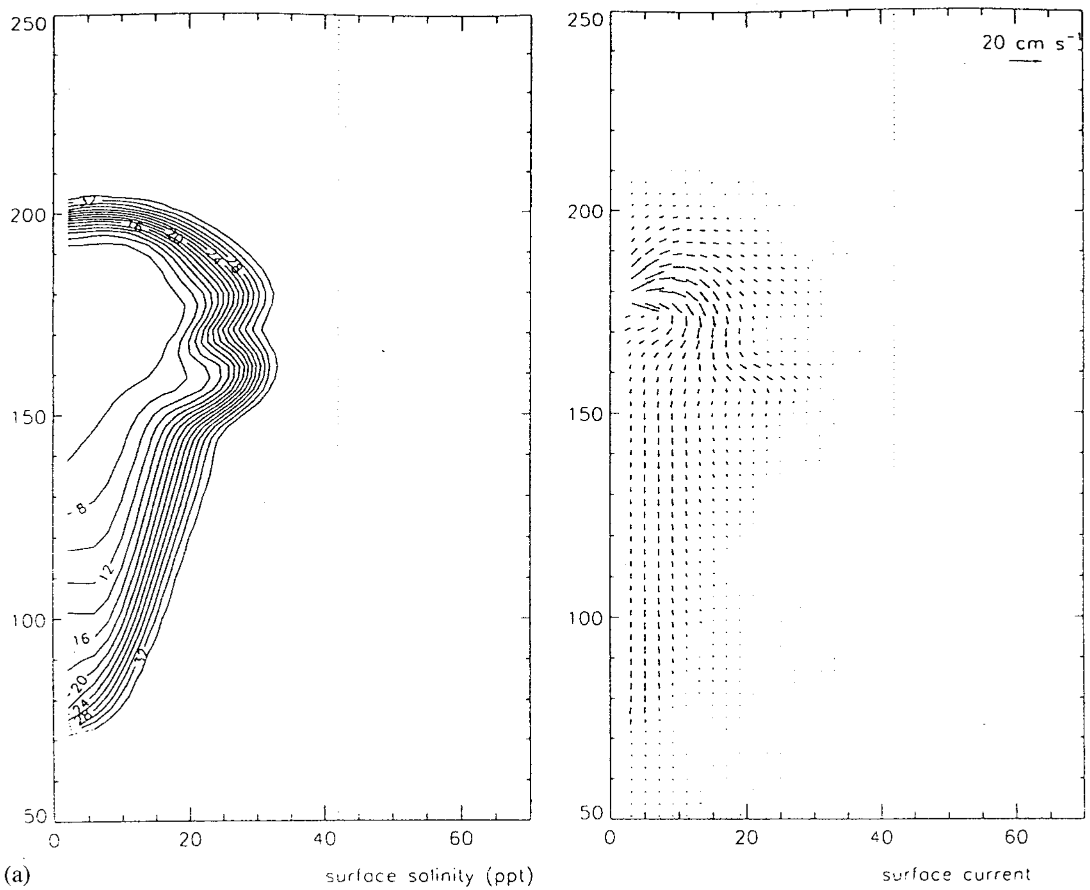

Figure 10. (a) As Figure 8(a) but with $A_v = 0.001$ $m^2 s^{-1}$ and $K_v = 0.00001$ $m^2 s^{-1}$ (calculation 9, Table I). (b) As Figure 8(b) but with $A_v = 0.001$ $m^2 s^{-1}$ and $K_v = 0.00001$ $m^2 s^{-1}$ (calculation 9, Table I).

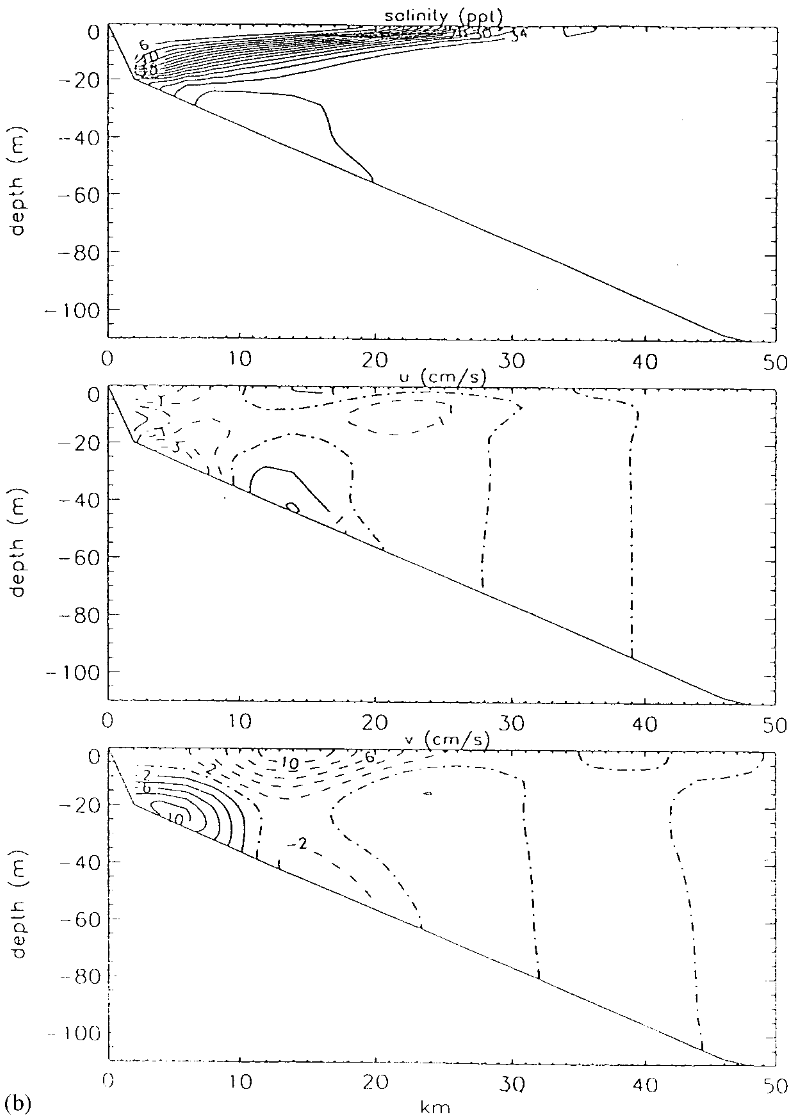

Figure 10 (*Continued*)

These calculation suggest that when K_v is high (taken of order 0.001 $\mathrm{m^2\,s^{-1}}$), the only effect of reducing A_v appears to be an increased tendency to produce a wave-like structure along the plume front, in particular to the north of the discharge point, and an increased current magnitude in this region.

Salinity contours at cross-section C_1, show a high level of vertical mixing (cf. Figure 12(b) and Figure 9(b)) comparable with that found previously with a high K_v value. The reduced value of A_v compared with calculation 8, leads to a change in the u current flow field along cross-section C_1, reflecting the local change in density gradients (Figure 12(a)). The spatial distribution of the v velocity is comparable with that found previously (cf. Figure 12(b) and Figure 9(b)), although the magnitude of the flow to the south at the surface and the return flow at depth has increased due to the reduction in vertical viscosity. This increase in surface flow to the south explains the slightly larger southerly spread of the plume (Figure 12(a)), compared with that found previously (Figure 9(a)).

This series of calculations shows that the horizontal spreading and vertical mixing of the plume is significantly influenced by K_v values, with changes in A_v producing similar effects, although the solution appears to be dominated more by changes in K_v than A_v. These results help to explain the differences between the turbulence energy models, and illustrate the importance of accurately determining K_v values in order to predict the movement of plumes. Equally, by accurately measuring the movement of a plume, and the associated forcing functions, namely discharge and wind fields together with far field flows that will advect the plume, it should be possible to determine the accuracy of various turbulence closure models. In these calculations the near coastal water depth was fixed at 20 m, in order to make comparisons with the constant depth solutions. Since the spread of the plume is largest in the near coastal region, in a final series of calculations, the authors will examine the sensitivity of the spread of the plume to changes in near shore water depth.

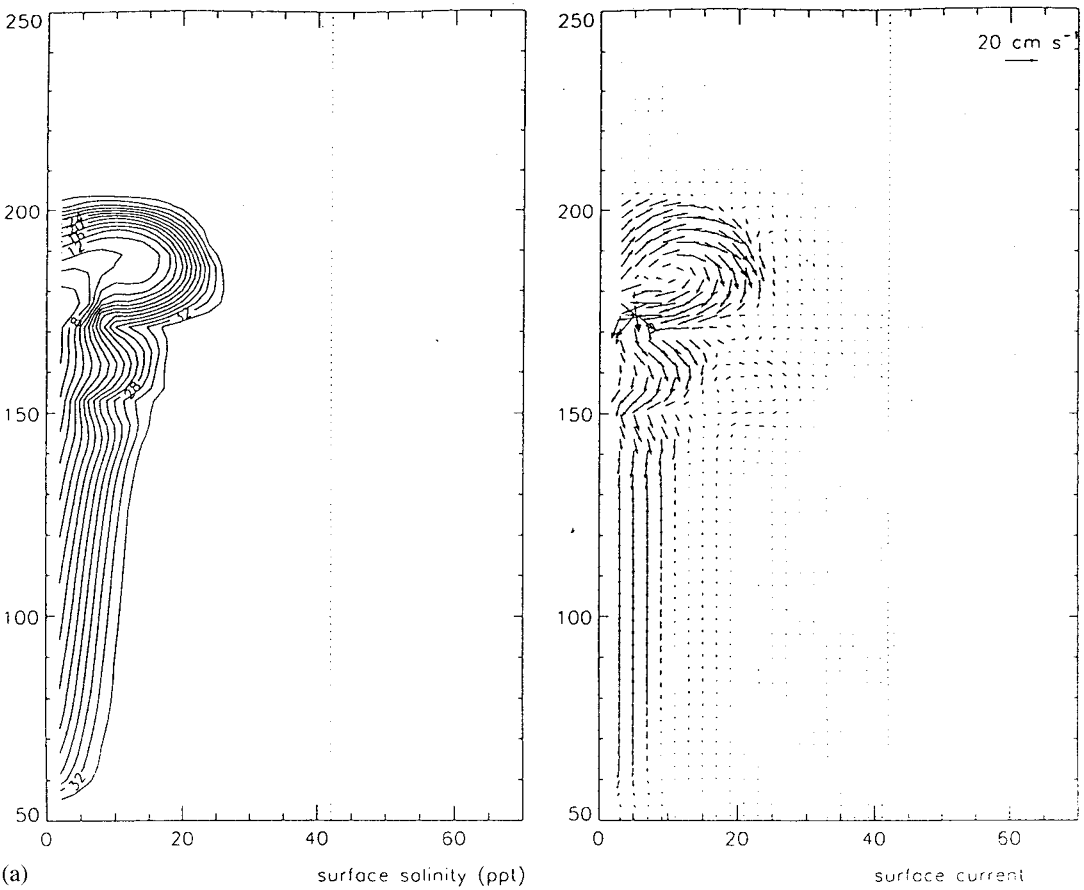

Figure 11. (a) As Figure 8(a) but with $A_v = 0.0001$ m^2 s^{-1} and $K_v = 0.0001$ m^2 s^{-1} (calculation 10, Table I). (b) As Figure 8(b) but with $A_v = 0.0001$ m^2 s^{-1} and $K_v = 0.0001$ m^2 s^{-1} (calculation 10, Table I).

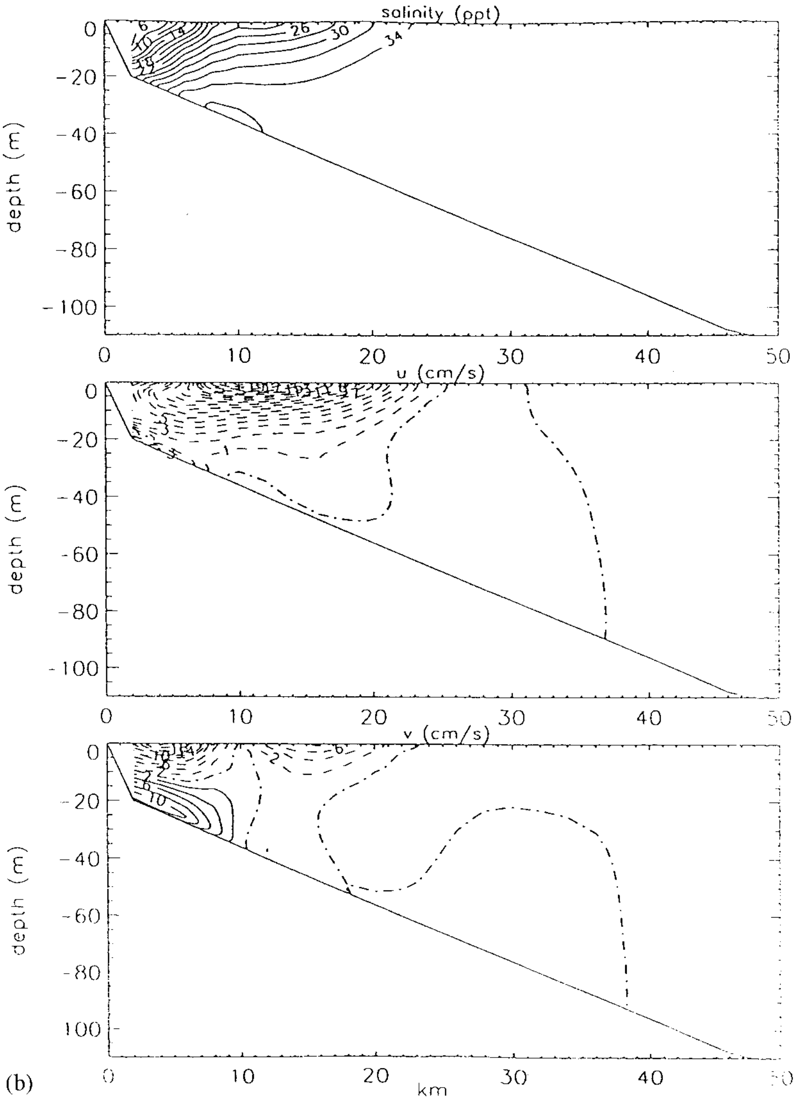

Figure 11 (*Continued*)

4.7. *Influence of near shore topography with $A_v = 0.001\ m^2 s^{-1}$, $K_v = 0.0001\ m^2 s^{-1}$ (calculation 12)*

In an initial calculation, using a near shore depth of 10 m (calculation 12) rather than the 20 m used previously, the A_v and K_v values were identical to those employed in calculation 7. Surface salinity contours (Figure 13(a)) show that the southward spread of the plume has been significantly reduced compared with that found previously (Figure 8(a)) due to the decrease in near shore depth. Also, the northward spread of the plume has increased. In essence the solution with the reduced water depth shows similar characteristics to that found by increasing the value of K_v. The reason for this can be understood by comparing salinity and current distributions at cross-section C_1 (Figure 8(b) and Figure 13(b)). In the shallow water case, the salinity gradient in the vertical is reduced compared with that found previously (a similar effect to that found by increasing K_v). Also, the magnitude of the across-shore and along-shore velocity components are reduced. The reduction in the magnitude of the southward surface flow is, however, different to that found previously when K_v is increased, and shows that although the spreading of the plume to the north is enhanced by reducing the water depth or increasing the K_v value, the southward movement is more sensitive to water depth changes than changes in K_v.

4.8. *Influence of near shore topography, with $A_v = 0.001$ m^2 s^{-1}, $K_v = 0.001$ m^2 s^{-1} (calculation 13)*

To confirm that the southward movement of the plume is influenced more by near shore water depths than K_v values, the previous calculation was repeated with K_v increased to 0.001 m^2 s^{-1} (calculation 13, Table I). Surface salinity contours (Figure 14(a)) show that the southward spread of the plume although slightly increased compared with Figure 13(a), is not appreciably different. However, the northerly spread of the plume has increased, and its off-shore spread decreased due to this change in K_v. The reason for this is that the vertical

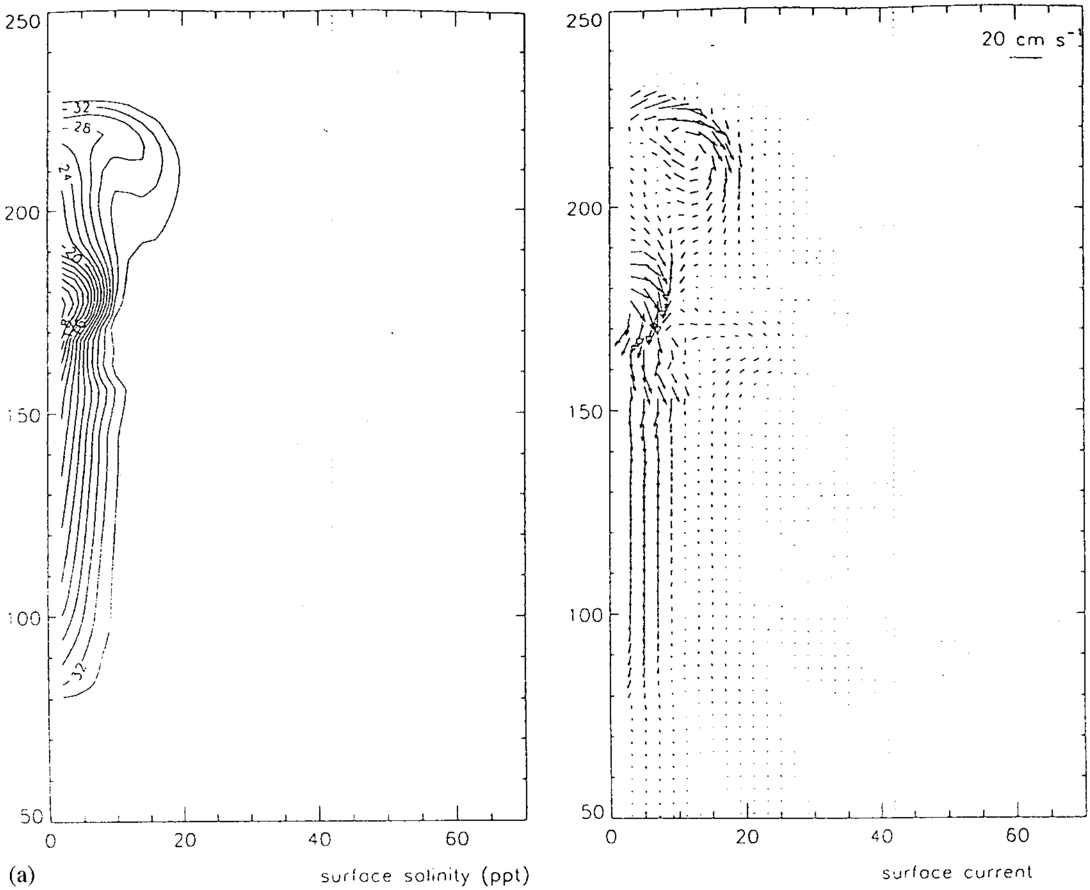

Figure 12. (a) As Figure 8(a) but with $A_v = 0.0001$ m^2 s^{-1} and $K_v = 0.001$ m^2 s^{-1} (calculation 11, Table I). (b) As Figure 8(b) but with $A_v = 0.0001$ m^2 s^{-1} and $K_v = 0.001$ m^2 s^{-1} (calculation 11, Table I).

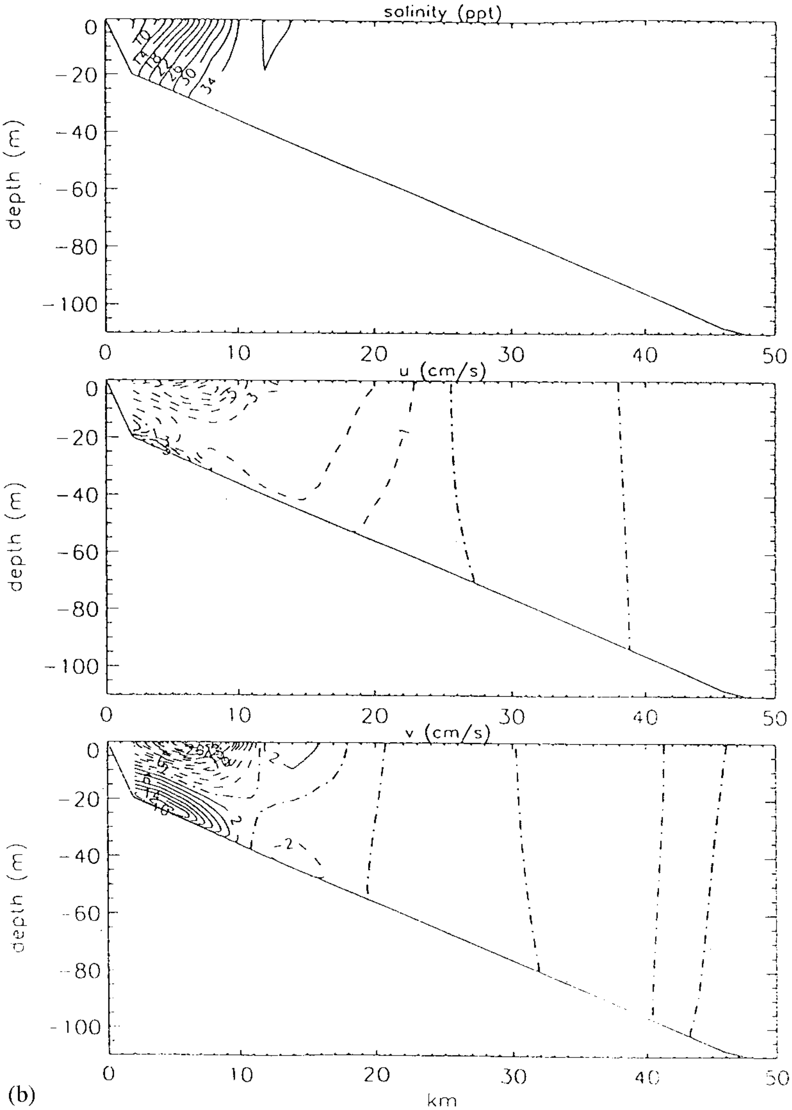

Figure 12 (*Continued*)

mixing has substantially increased in the near shore region due to the increase in K_v (cf. Figure 14(b) and Figure 13(b)).

These calculations suggest that the southward spread of the plume in a shallow water case is only slightly influenced by the value of K_v, and is largely determined by near shore water depth. If the plume front away from the discharge point in the near shore region moves at a speed primarily determined by $(gh)^{1/2}$, with g the gravitational constant, and h taken as near coastal water depth, then changing h from 10 to 20 m, should mean that the plume propagates further south by a factor of approximately 1.4. In the case of $h = 10$ m, the plume has propagated about 65 km to the south of the discharge point. Using a factor of 1.4 to scale this distance, predicts that for $h = 20$ m, the plume should have spread 91 km from its discharge point, which approximates the southward spread of the plume found in calculation 7 (Figure 8(a)). This suggests that an accurate knowledge of near shore topography is required to predict the southward spread of the plume, although measurements of this spread may not be a critical test of the accuracy of K_v values in the model. The more critical test and hence more important measurements in this case will be the northward and off-shore spread of the plume, although these will also be influenced by topography that will need to be accurately specified in any prediction model before any conclusions can be drawn concerning K_v values from model and observation comparisons.

5. CONCLUDING REMARKS

In this paper the authors have briefly described the major steps in developing a three-dimensional model that can be used in the study of plume dynamics. The model uses an accurate and gradient preserving advection scheme, namely the total variation diminishing, TVD method [39] for density advection, and hence can accurately represent the density discontinuity associated with the movement of the plume front.

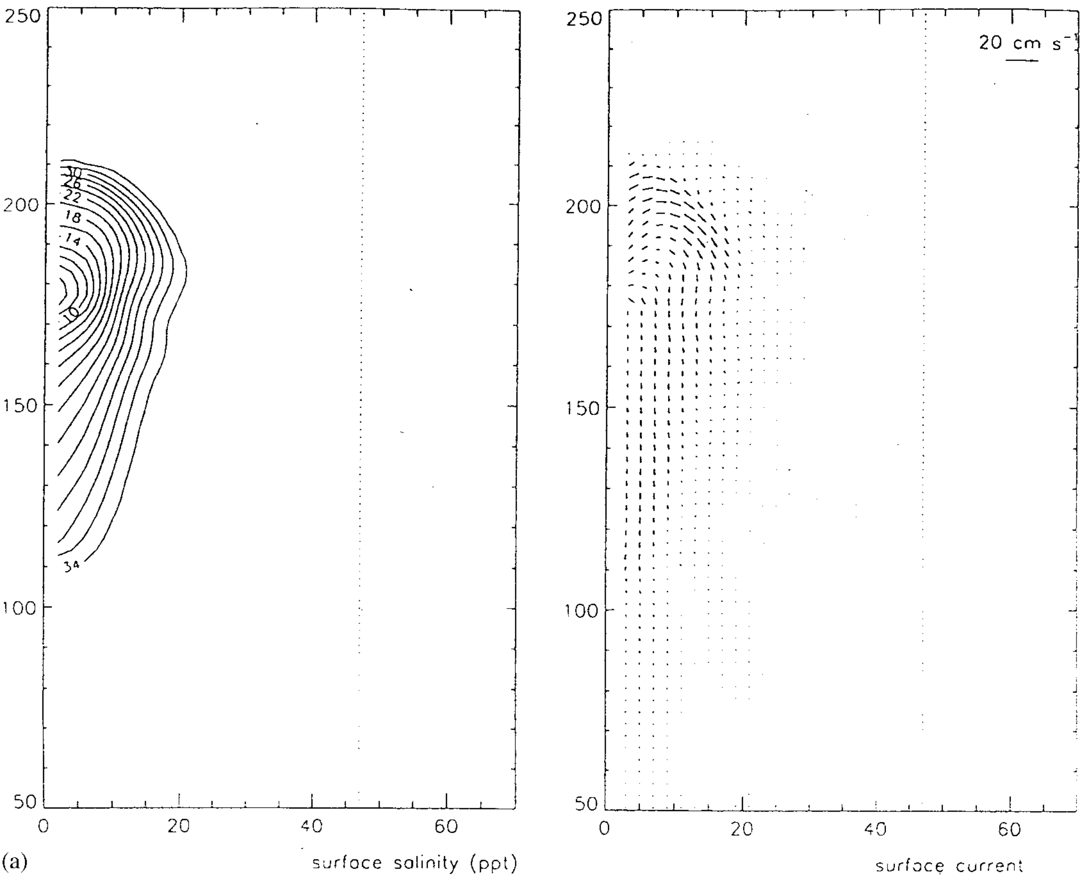

Figure 13. (a) As Figure 8(a) but with $A_v = 0.001$ m^2 s^{-1} and $K_v = 0.0001$ m^2 s^{-1} and a sloping bottom but with a near coastal water depth of 10 m (calculation 12, Table I). (b) As Figure 8(b) but with $A_v = 0.001$ m^2 s^{-1} and $K_v = 0.0001$ m^2 s^{-1} and a sloping bottom but with a near coastal water depth of 10 m (calculation 12, Table I).

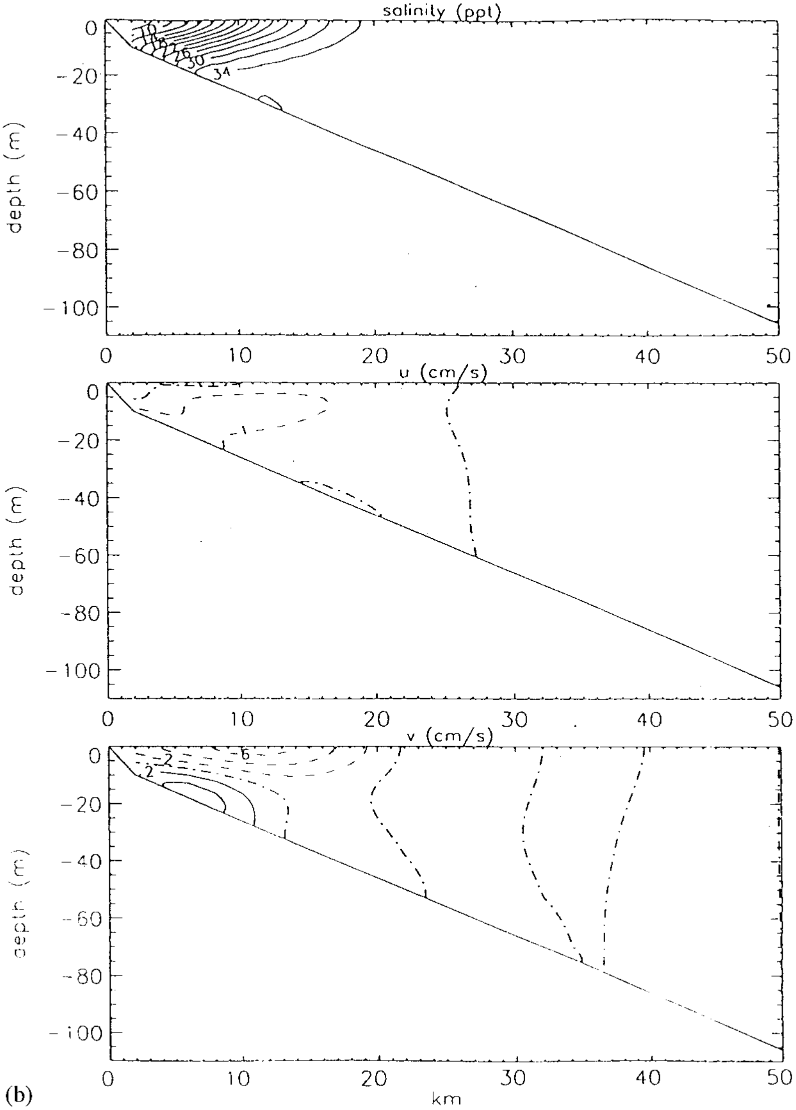

(b)

Figure 13 (*Continued*)

By using two different, although widely accepted, turbulence energy models to parameterize the vertical mixing of momentum and density, it has been possible to examine the sensitivity of spreading and mixing of the plume to the parameterization of subgrid scale processes.

Initial calculations using a fixed discharge rate, and salinity difference between the plume and surrounding sea water, with water depth constant at $h = 20$ m, showed that although both turbulence energy models gave plumes with similar spatial features (namely both were supercritical), the southward and off-shore extent of the plumes were different, with measurable differences in the magnitude of surface currents, which could be detected with shore based HF Radar measurements.

Although cross-sectional plots showed similar spatial distributions of the u and v velocity fields, the salinity distributions were different, particularly the vertical extent of the mixing in the near shore region. This suggests that a detailed and highly accurate set of current measurements would be required to distinguish between the two parameterizations of mixing, which is difficult to achieve with limited field measurements. However, the significant differences in the salinity fields suggests that, detailed surveys of this parameter may distinguish between the models.

Although the turbulence energy models are a better description of the physical mixing than fixed viscosity (A_v) and diffusivity (K_v) values, calculations using prescribed values of these parameters revealed their importance in determining plume characteristics and the spread of the plume. The general trends found in the calculations are summarized in Table II. From the calculations and the summary in Table II, it is found in essence increasing A_v and K_v reduced the southerly spread of the plume, with a large A_v value producing a plume that spreads both northward and southward to a similar extent. Also, increasing A_v and K_v tends to reduce the off-shore spread of the plume, with increasing K_v enhancing the vertical extent of the plume. Also, there appears to be a tendency for the plume to change from supercritical to subcritical,

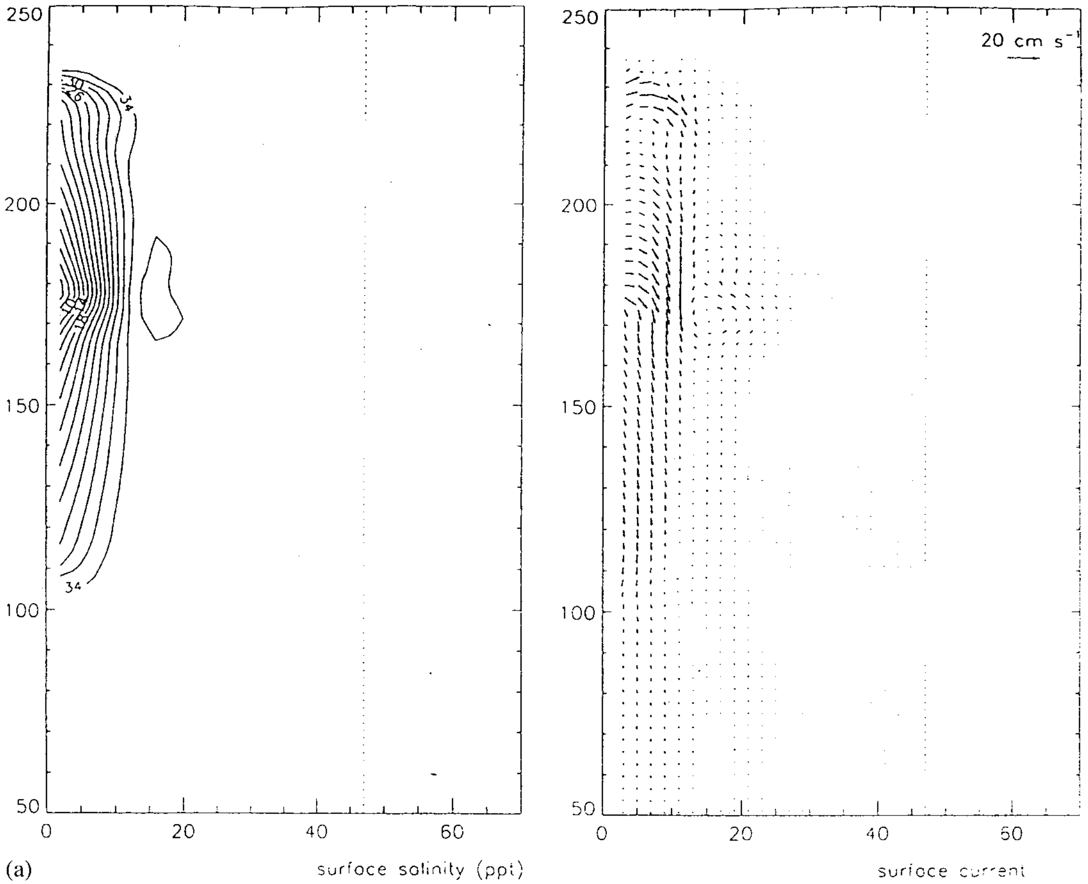

Figure 14. (a) As Figure 8(a) but with $A_v = 0.001$ m^2 s^{-1} and $K_v = 0.001$ m^2 s^{-1} and a sloping bottom but with a near coastal water depth of 10 m (calculation 13, Table I). (b) As Figure 8(b) but with $A_v = 0.001$ m^2 s^{-1} and $K_v = 0.001$ m^2 s^{-1} and a sloping bottom but with a near coastal water depth of 10 m (calculation 13, Table I).

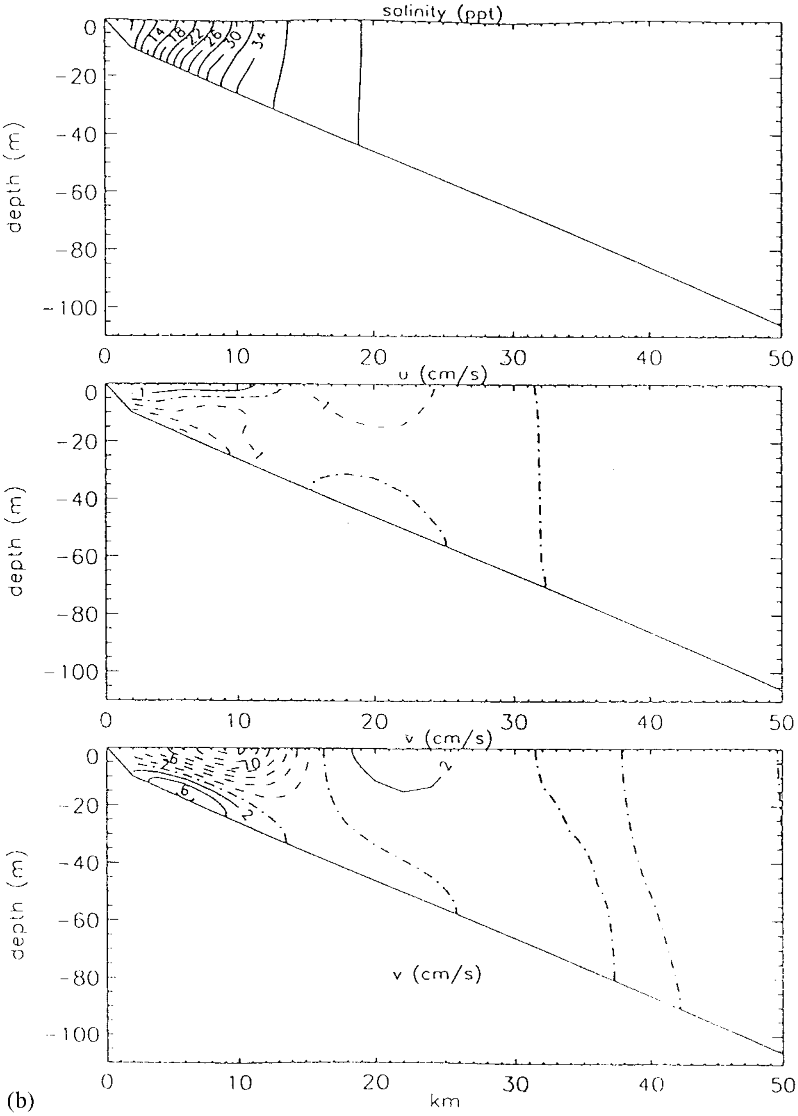

Figure 14 (*Continued*)

and eventually to show a nearly uniform spread in the region of the discharge point as A_v and K_v are increased. Associated with these changes is a decrease in frontal meanders and baroclinic instability.

The reason for these changes in plume characteristics is probably due to local pressure gradients and frictional effects. In the absence of strong vertical mixing for a given discharge width, the off-shore extent of the plume is determined by discharge velocity and rotation and in essence is supercritical. However, when significant vertical mixing occurs close to the discharge point, the water column in the area of the discharge becomes well-mixed, and there is a local horizontal pressure gradient that prevents the off-shore spread. This situation gives rise to a uniform spreading in the region of the discharge point, with no enhanced spreading to the south. Between these two extremes is a situation where the off-shore spreading is reduced in the region of the discharge but spreading occurs to the south, where increased off-shore spreading occurs on the short time scale before vertical mixing dominates. This situation gives rise to a subcritical plume.

The calculations using an off-shore sloping topography, clearly show that topographic effects can be more important in the spread of the plume than the differences between the one-equation and two-equation turbulence energy models, suggesting that in order to differentiate between these two models, besides surface current measurements from an HF Radar, and detailed salinity surveys, an accurate representation of topography is essential. Calculations clearly showed that in the case of the sloping bottom, the vertical mixing was reduced with distance from the coast due to the increasing separation of surface and bed mixed layers.

The calculations with the constant values of A_v and K_v in the sloping bottom case, showed similar results to those found previously with a flat bottom, namely that increased values of A_v and K_v produced subcritical plumes, with for a fixed value of A_v, the northward extent increased, and the off shore extent decreased as K_v is increased.

A summary of the general effects upon the dynamics of the plume, in changing from a constant water depth to a depth that increases off shore, and reducing the near shore depth is given in Table II. In essence, for a fixed A_v and K_v, changing from the constant depth case to one involving an off shore increase in depth, had the effect of decreasing the off-shore extent of the plume, due to vorticity constraints, leading to an increased southerly extent. Vorticity constraints also reduced the off-shore meanders and baroclinic instabilities associated with the

Table II. A simplified summary of the major conclusions from the calculations

Constant depth calculations				
Property of plume	Low A_v, K_v	→		High A_v, K_v
Southerly extent		Reduced	→	
Northerly extent		Increased	→	
Off-shore extent		Reduced	→	
	(Can depend on A_v and K_v values and bottom topography)			
Vertical extent		Increased	→	
Plume features	Subcritical	→		Subcritical
Off-shore meanders and instability		Reduced	→	
Varying depth calculations				
Property of plume	Constant depth		→	Depth increasing off shore
Southerly extent		Increased	→	
Off shore extent		Reduced	→	
Vertical extent		Reduced	→	
Plume features	Supercritical	→		Subcritical
Off-shore meanders and instability		Reduced	→	
Varying depth near shore				
Property of plume	Deep near shore	→		Shallow near shore
Southerly extent		Reduced	→	
Northerly extent		Increased	→	

plume front and increased the tendency for the plume to exhibit subcritical behaviour. The vertical extent of the surface boundary layer is also affected by depth changes (Table II). The reason for this is that as the water depth increases off shore, the surface boundary layer associated with the plume is removed from the effects of turbulence in the bottom boundary layer, and consequently its vertical extent is reduced.

The effect of a decrease in near shore water depth is to reduce the southerly spread of the plume with an associated increase in its northerly extent (Table II).

This series of calculations has clearly shown that the spread of the Ebro plume is not only related to the larger scale features such as discharge rate, internal Rossby radius of deformation, and Froude number which have been identified in previous plume studies, but is significantly influenced by the parameterization of vertical mixing. By using models in which A_v and K_v values have been specified it is possible to determine that each has a significant influence upon the spread of the plume, and by this means to understand the differences that arise by using one-equation or two-equation turbulence models. Calculations using the turbulence energy models with a flat bottom and a sloping bottom, illustrate the differences in vertical mixing due to surface and bed boundary layers overlapping in the flat bottom case, and their separation in the sloping bottom case.

In the one-equation model considered here, the mixing length was specified algebraically and did not take account of stratification effects that lead to a reduction in its value [26], and give results comparable with a two-equation model [42]. Although a detailed discussion of the range of turbulence energy models that exist in the literature [24] is not possible here, it is clear from the calculations performed in this paper that turbulence models that produce low values of A_v and K_v in stratified flows when applied to plume dynamic problems will show similar plume features to those found with the two equation model. However, if the turbulence model gives rise to significantly higher values of A_v and K_v, then the computed plume will correspond to that determined with the one-equation model.

Although a very detailed set of measurements will be required to differentiate between the one-equation and two-equation turbulence models, the sensitivity of the spread of the plume to A_v and K_v values should enable appropriate values of these parameters to be indirectly determined from HF measurements of surface currents, and salinity surveys of the vertical and the horizontal spread of the plume.

ACKNOWLEDGMENTS

This work was carried out as part of the FANS project. It was supported by the EC MAST Research Programme, Directorate General for Science, Research and Development under contract No. MAS3-CT95-0037, DG12-ESCY. The authors are indebted to Mr R.A. Smith for preparing diagrams and Mrs L. Ravera and Mrs C. Burke for typing the paper.

REFERENCES

1. T.W. Kao, 'The dynamics of small scale fronts, I. Shelf water structure due to fresh water discharge', *J. Phys. Oceanogr.*, **11**, 1215–1223 (1981).
2. T.W. Kao, C. Park and H.-P. Pao, 'Buoyant surface discharge and small-scale oceanic fronts: A numerical study', *J. Geophys. Res.*, **82**, 1747–1752 (1977).
3. T.A. McClimans, 'Estuarine fronts and river plumes', in J. Dronkers and W. Van Leussen (eds.), *Physical Processes in Estuaries*, Springer, New York, 1986, pp. 56–69.
4. J.O. Blanton, 'Oceanic currents along a near shore frontal zone on the continental shelf of the south eastern United States', *J. Phys. Oceanogr.*, **11**, 1627–1637 (1981).

5. J.O. Blanton, F.E. Werner, C. Kim, L.P. Atkinson, T.N. Lee and D. Savidge, 'Transport and fate of low-density water in a coastal frontal zone', *Cont. Shelf Res.*, **14**, 401–427 (1994).
6. D.A. Brooks, 'A model study of the buoyancy-driven circulation in the Gulf of Maine', *J. Phys. Oceanogr.*, **24**, 2387–2412 (1994).
7. S.Y. Chao, 'River-forced estuarine plumes', *J. Phys. Oceanogr.*, **18**, 72–88 (1988).
8. V.H. Kourafalou, L.-Y. Oey, J.D. Wang and T.N. Lee, 'The fate of river discharge on the continental shelf. 1. Modelling the river plume and the inner shelf coastal current', *J. Geophys. Res.*, **101**, 3415–3434 (1996).
9. P.J. Luyten, E.L. Deleersnijder, J. Ozer and K.G. Ruddick, 'Presentation of a family of turbulence closure models for stratified shallow water flows and preliminary application to the Rhine outflow region', *Cont. Shelf Res.*, **16**, 101–130 (1996).
10. J. Salat, 'The interaction between the Catalan and Balearic currents in the southern Catalan Sea', *Oceanol. Acta*, **18**, 227–234 (1995).
11. J. Font, E. G.-Ladona and E.G. Gorriz, 'The seasonality of mesoscale motion in the Northern current of the western Mediterranean: several years of evidence', *Oceanol. Acta*, **18**, 207–219 (1995).
12. P.E. La Violette, J. Tintoré and J. Font, 'The surface circulation of the Balearic Sea', *J. Geophys. Res.*, **95**, 1559–1568 (1990).
13. M. Espino, A. S.-Arcilla and M.A. Garcia, 'Wind induced mesoscale variability of the shelf circulation off the Ebro delta, NW Mediterranean: a numerical study', *J. Marine Syst.*, **16**, 235–251 (1998).
14. J.-M. Pinot, J. Tintoré and D. Gomis, 'Multivariate analysis of the surface circulation in the Balearic Sea', *Prog. Oceanogr.*, **36**, 343–376 (1995).
15. J. Font, J. Salat and A. Julia, 'Marine circulation along the Ebro continental margin', in C.H. Nelson and A. Maldonado (eds.), *Marine Geology of the Ebro Continental Margin*, *Mar. Geol.*, **95**, 165–177 (1990).
16. J.P. Matthews, A.D. Fox and D. Prandle, 'Radar observation of an along-front jet and transverse flow convergence associated with a North Sea front', *Cont. Shelf Res.*, **13**, 109–130 (1993).
17. R.W. Garvine, 'Estuary plumes and fronts in shelf waters: a layer model', *J. Phys. Oceanogr.*, **17**, 1877–1896 (1987).
18. D.P. Wang, 'Mutual intrusion of gravity current density front formation', *J. Phys. Oceanogr.*, **14**, 1191–1199 (1984).
19. R.L. Haney, 'On the pressure gradient force over steep topography in sigma co-ordinate ocean models', *J. Phys. Oceanogr.*, **21**, 610–619 (1991).
20. G.S. Stelling and J.A.T.M. Van-Kester, 'On the approximation of horizontal gradients in sigma co-ordinates for bathymetry with steep bottom slopes', *Int. J. Numer. Methods Fluids*, **10**, 915–937 (1994).
21. A.D. Heathershaw, J. Small and C.E. Stretch, 'Frictional formulations in numerical ocean models and their effect on simulated acoustic fields', *J. Phys. Oceanogr.*, **24**, 274–297 (1994).
22. J. Xing and A.M. Davies, 'Internal lee waves and turbulence mixing over an isolated seamount: results from turbulence energy models', *Int. J. Numer. Methods Fluids*, **23**, 1043–1072 (1996).
23. A.M. Davies, J.E. Jones and J. Xing, 'Review of recent developments in tidal hydrodynamic modelling. 1: Spectral models', *J. Hydraul. Eng.*, **123**, 278–292 (1997).
24. A.M. Davies, J.E. Jones and J. Xing, 'Review of recent developments in tidal hydrodynamic modelling. 2: Turbulence energy models', *J. Hydraul. Eng.*, **123**, 293–302 (1997).
25. J. Xing and A.M. Davies, 'Application of a range of turbulence energy models to the determination of M_4 tidal current profiles', *Cont. Shelf Res.*, **16**, 517–547 (1996).
26. J. Xing and A.M. Davies, 'The influence of mixing length formulation and stratification upon tidal currents in shallow seas', *Estuar. Coast. Shelf Sci.*, **42**, 417–456 (1996).
27. A.F. Blumberg and G.L. Mellor, 'A description of a three-dimensional coastal ocean circulation model', in N.S. Heaps (ed.), *Three-dimensional Coastal Ocean Models*, 208 pp., American Geophysical Union, Washington DC, 1987, pp. 1–16. (*Coast. Estuar. Sci.*).
28. L.-Y. Oey and P. Chen, 'A nested-grid ocean model: with application for the simulation of meanders and eddies in the Norwegian coastal current', *J. Geophys. Res.*, **97**, 20063–20086 (1992).
29. L.-Y. Oey and P. Chen, 'A model simulation of circulation in the Northeast Atlantic Shelves and Seas', *J. Geophys. Res.*, **97**, 20087–20115 (1992).
30. H. Baumert and G. Radach, 'Hysteresis of turbulent kinetic energy in non-rotational tidal flows: a model study', *J. Geophys. Res.*, **97**, 3669–3677 (1992).
31. B. Galperin, L.H. Kantha, S. Hassid and A. Rosati, 'A quasi-equilibrium turbulent energy model for geophysical flows', *J. Atmos. Sci.*, **45**, 55–62 (1988).
32. B. Galperin, A. Rosati, L.H. Kantha and G.L. Mellor, 'Modelling rotating stratified turbulent flows with application to oceanic mixed layers', *J. Geophys. Res.*, **19**, 901–916 (1989).
33. P.J. Luyten, 'An analytical and numerical study of surface and bottom boundary layers with variable forcing and application to the North Sea', *J. Mar. Syst.*, **8**, 171–190 (1996).
34. A.G. Davies, R.L. Soulsby and H.L. King, 'A numerical model of the combined wave and current bottom boundary layer', *J. Geophys. Res.*, **93**, 491–508 (1988).
35. A.M. Davies, 'On using turbulence energy models to develop spectral viscosity models', *Cont. Shelf Res.*, **11**, 1313–1353 (1991).

36. A.M. Davies and J.E. Jones, ‘Application of a three-dimensional turbulence energy model to the determination of tidal currents on the northwest European shelf’, *J. Geophys. Res.*, **95**, 18143–18162 (1990).
37. A.M. Davies and J.E. Jones, ‘On the numerical solution of the turbulence energy equations for wave and tidal flows’, *Int. J. Numer. Methods Fluids*, **12**, 17–41 (1991).
38. B. Johns and T. Oguz, ‘Turbulent energy closure schemes’, in N.S. Heaps (ed.), *Three-dimensional Coastal Ocean Models*, AGU, 1987.
39. J. Xing and A.M. Davies, ‘The influence of wind effects upon internal tides in shelf edge regions’, *J. Phys. Oceanogr.*, **27**, 2100–2125 (1997).
40. A.M. Davies and J. Xing, ‘An intercomparison and validation of a range of turbulence energy schemes used in three-dimensional tidal models’, in D.R. Lynch and A.M. Davies (eds.), *Qualitative Skill Assessment for Coastal Ocean Models*, AGU Coastal and Estuarine Series, 1995, pp. 71–95.
41. E.A. Martinsen and H. Engedahl, ‘Implementation and testing of a lateral boundary scheme as an open boundary condition in barotropic ocean models’, *Coast. Eng.*, **11**, 603–627 (1987).
42. J. Xing and A.M. Davies, ‘Application of a range of turbulence energy models to the computation of the internal tide’, *Int. J. Numer. Methods Fluids*, **26**, 1055–1084 (1998).